Correlative analysis of interaction between recrystallization and precipitation during sub-critical annealing of cold-rolled low-carbon V and Ti-V bearing microalloyed steels

Ishwar Kapoor[a,*], Yongjun Lan[b], Arjan Rijkenberg[c], Geoff West[a], Zushu Li[a] and Vit Janik[a, d]

[a] *WMG, University of Warwick, Coventry, CV4 7AL, UK;*

[b] *Tata Steel, Coventry Technology Centre, Coventry, CV4 7EZ, UK;*

[c] *Tata Steel, 1970 CA IJmuiden, The Netherlands;*

[d] *Institute for Future Transport and Cities, Coventry University, Coventry, CV1 5FB, UK*

*Corresponding author at: WMG, University of Warwick, Coventry, CV4 7AL, UK

E-mail addresses: Ishwar.Kapoor@warwick.ac.uk (I.Kapoor), yongjun.lan@tatasteeleurope.com (Y.Lan), arjan.rijkenberg@tatasteeleurope.com (A. Rijkenberg), g.west@warwick.ac.uk (G.West), z.li.19@warwick.ac.uk (Z.Li) and ac6600@coventry.ac.uk (V.Janik)

Abstract

In this paper a new insight into fundamentals of static recrystallization, precipitation and their interaction during sub-critical annealing of three cold-rolled low-carbon microalloyed steel grades is presented. The grades under investigation are a base grade containing V as a microalloying element, a Ti+ grade containing Ti as microalloying element added into the base grade, and a Ti+Mn+ grade containing additional Mn added into the Ti+ grade. The cold-rolled steels are sub-critically annealed inside a muffle furnace to simulate industrial continuous annealing parameters in order to investigate the interaction between recrystallization and precipitation across transient stages of the annealing process as a function of temperature and time. The Zener pinning of precipitates and solute drag force of Mn on the recrystallization process are calculated and compared with measured values obtained from experimental studies on the recrystallization kinetics. Results suggest that the recrystallization kinetics is fastest in the base grade. For the Ti+ grade, fine (< 15 nm) (Ti,V)(C/N) particles retard the recrystallization kinetics. For the Ti+ and Ti+Mn+ grades, solute drag effect of Mn solute atoms for dwell time longer than 2 min at annealing temperature of 800 °C is negligible.

Keywords: annealing; recovery; recrystallization; microalloyed steel; precipitation; solute drag

1. Introduction

Development of light-weight automotive body structures is crucial nowadays in automotive industry to minimise car fuel consumption and greenhouse gases emissions [1,2]. The 2017 UK greenhouse gas annual report revealed that transport sector accounts for ~ 34 % of the total CO_2 emissions. Passenger cars within road transport section are the most significant source of CO_2 emissions [3]. In order to minimise CO_2 emissions from cars, countries such as Norway, Sweden and the UK are working on

shifting petrol and diesel automotive powertrain to a complete zero emissions Electric Vehicle (EV) powertrain [4]. As a result of that, lithium batteries and related gadgets are incorporated into electric, hybrid, solar or hydrogen driven cars, necessitating radical light-weighting of automotive structures to offset weight gain due to added energy storage [5]. Therefore, at present, vehicle light-weighting (including petrol, diesel or electric vehicles) is one of the top priorities in automotive industry, with various alternative materials for car bodies investigated, including aluminium [6], magnesium [7], steel [8], polymers and polymer-based or carbon-based composites [9], and their combinations (hybrid materials) [10].

Among engineering materials, steel is widely used in automobiles because of its abundance, cost effectiveness and ease in manufacturing capability as compared to other materials [11,12]. Hot-rolled dual-phase (DP) and complex-phase (CP) steels are exhaustively used for chassis and suspension systems because of their high strength and excellent formability at low capital costs [13–15]. In case of multi-phase steels, the amount of second-phase particles such as pearlite, bainite or martensite together with ferrite is significant in terms of providing increased strength, but limits the formability and flexibility of these materials during forming [8,16–20]. To resolve stress accumulation failure issues during plastic deformation, a single phase ferrite matrix grade with nanometre-sized precipitates has been developed mainly for chassis and suspension applications with excellent stretch flange formability [8,19]. Funakawa et al. [19] developed hot-rolled steel of single phase ferrite matrix with (Ti, Mo)C fine precipitates of 4-6 nm in diameter which provides additional strength of about 300 MPa from precipitation hardening. Yi et al. [21] investigated Ti-V-Nb microalloyed single phase ferrite hot-rolled steel. Because of the cumulative strengthening from precipitation (~ 250 MPa); dislocations (~ 145 MPa) and solid solution strengthened ferrite base matrix (~ 315 MPa), hot-rolled steel of average yield strength of about 710 MPa is achieved [21]. Similarly, Rijkenberg et al. [8] have developed hot-rolled steel grades with single phase ferrite matrix microalloyed with Nb-V-Mo elements. A combination of random and fine (~ 3 nm) interphase precipitates of V, NbV and NbVMo carbon-nitrides leads to enhanced precipitation strengthening (200 MPa to 450 MPa) in these steel grades.

Microalloying content of Nb, Ti, V or Mo in low-carbon microalloyed steel grades is limited to avoid inhibition of recrystallization and maintain precipitation strengthening [22–29]. Static recrystallization and precipitation behaviour of cold-rolled low-carbon microalloyed steel during sub-critical annealing in the fully ferritic region is relatively less understood as compared to dynamic recrystallization during hot rolling of austenite. Cold-rolled continuously-annealed (CA) low-carbon microalloyed steel (TS > 600 MPa) with single ferrite phase matrix containing nanometre-sized precipitates [8,30] for BIW applications is a new concept that requires further investigations of recovery and recrystallization of cold-rolled textures with varied stored energy as well as the interaction of precipitates with microstructural defects.

The purpose of this paper is to develop a correlative material characterisation technique combining EBSD and FIB-lift out STEM to fundamentally understand the precipitation evolution and their interaction with recrystallization during sub-critical annealing of three novel cold-rolled low-carbon microalloyed steel grades: a) base grade containing V as microalloying element; b) Ti+ grade containing increased Ti as microalloying element; and c) Ti+Mn+ grade containing additional Mn and Ti.

2. Experimental Procedures

2.1. Preparation of investigated materials

The chemical compositions of the investigated steel grades are shown in the Table 1. As-cast steel blocks with thickness ~ 30 mm were heated at Tata Steel Europe Research & Development facilities in a laboratory scale muffle furnace at T ~ 1200 °C, manually descaled to remove any oxide layers and manually rolled in between a set of two rollers up to the thickness of 3 mm. The final rolling temperature ~ 890 °C was recorded by a pyrometer. To simulate the industrial run-out-table cooling practise, the strips were transferred to a run-out-table, where a combination of air and water was used to cool the strips to a temperature of ~ 580 °C to avoid interphase and random precipitation and to ensure that all austenite grains are transformed to ferrite. Strips were then transferred to a cooling furnace for a controlled slow cooling to room temperature to replicate coiling and slow coil cooling. Selected hot-rolled steel sheets (500 mm x 110 mm x 3 mm) were taken out from the processing route for precipitate investigation using TEM and the rest hot-rolled steel sheets were manually cold-rolled at room temperature to the final thickness of 1 mm with ~ 70 % reduction in thickness.

Table 1: Chemical composition in weight (%) for the three grades of steel investigated in this study

Grades	C	Si	**Mn**	P	S	Al	**V**	**Ti**	N
Base	0.051	0.008	0.34	0.001	0.0009	0.033	0.15	-	0.0028
Ti+	0.051	0.007	0.34	0.001	0.0007	0.032	0.15	0.078	0.0022
Ti+Mn+	0.051	0.007	0.89	0.001	0.0009	0.030	0.15	0.075	0.0031

2.2. Muffle furnace annealing

Samples with dimensions of 6 mm × 6 mm × 1 mm were cut from the centre of the as-received cold rolled sheet (Fig. 1) and annealed in a muffle furnace under following conditions: 700 °C 0 s, 800 °C 0 s; 800 °C 2 min; 800 °C 5 min; 800 °C 15 min; 800 °C 30 min; 800 °C 1 h and 800 °C 2 h. Heating rate was controlled to 10 – 15 °C /s. To simulate quick thermal response of the sample, a preheated metal block was kept inside the heated furnace for ~ 30 min. A 'K type' thermocouple reader coupled with data logger was fitted inside the furnace to record the surface temperature of the metallic block. The temperature difference between the metallic block and the muffle furnace (measured by inbuilt

thermocouple) was recorded as 5 °C. As the target temperature was achieved, the muffle furnace was opened, the test sample was placed on the metallic block and the furnace door were closed immediately to prevent temperature from dropping. The temperature was recorded throughout the annealing cycle. Once the required annealing temperature and dwell time were achieved, the doors were opened and the sample was taken out to be air cooled to room temperature. The various annealing conditions (mentioned above) are designed in this work for the purpose to study the effect of microalloying elements on the recrystallized microstructure development and on the mechanical properties.

2.3. Microstructural characterisation

For the microstructural study, the muffle furnace annealed samples (6 mm x 1 mm x 1mm) were cut in half in direction parallel to the RD-ND plane (Fig. 1), mounted in Bakelite and polished using standard metallographic techniques for microstructural investigation in the transverse (TD) direction. Polished samples were placed on the stage inside SEM with the Rolling Direction (RD) parallel to X-axis, Transverse direction (TD) parallel to Z-axis and Normal direction (ND) parallel to Y axis of the stage coordinate axis system inside of the SEM chamber. FEG-SEM Carl Zeiss fitted with NordlysNano EBSD camera by Oxford Instruments [31] was used. FIB lift-outs were performed from the un-recrystallized and recrystallized ferrite matrix of cold-rolled and annealed samples for conditions: 700 °C 0 s, 800 °C 0 s; 800 °C 2 min; 800 °C 5 min and studied under TEM to investigate precipitate size and distribution. FIB-lift outs were also performed from the ferrite matrix of hot-rolled samples (RD-ND plane) taken from the centre of hot-rolled sheet and studied under TEM to investigate the precipitate distribution. Parameters and equipment employed for the EBSD data acquisition, FIB lift-out and TEM investigations were the same as used in previous work by Kapoor et al. [32].
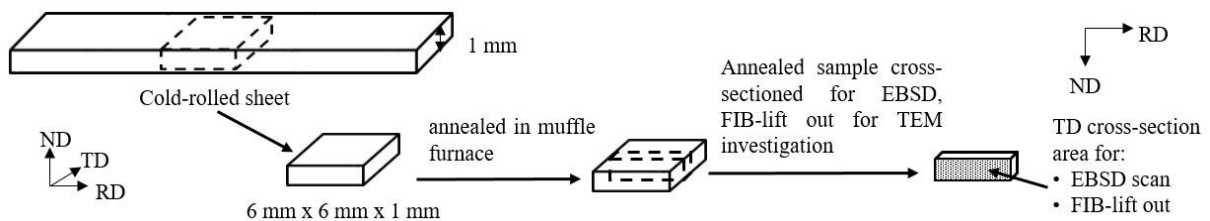

Fig. 1 Sample geometry for muffle furnace annealing, EBSD and FIB-lift out investigation

Obtained EBSD data were exported to Channel 5 software of Oxford Instruments to evaluate:

- Normal direction Inverse Pole Figure (ND-IPF) maps
- Local Average Misorientation (LAM) data of kernel size 7 x 7
- LAM map was exported to MTEX-4.5.0 toolbox in MATLAB to evaluate noise free Geometrically necessary dislocation (GND) density applying the same methodology as mentioned by Kapoor et al. [32], Moussa et al. [33] and Calcagnotto [34].
- 2D Orientation Distribution Function (ODF) texture data on the section $\varphi_2 = 45°$ from a low magnification x 250 scanned RD-ND section of the sample

The degree of recrystallization (%) was evaluated using three different methods: LAM, Vickers hardness (HV) and Aspect Ratio of grain. Microstructural area with LAM < 1° were characterised as recrystallized [35]. The area fraction of the scanned map consisting of pixels with average misorientation < 1° was calculated to evaluate the recrystallized fraction. Hardness of the samples for cold-rolled, fully recrystallized and intermediate conditions were evaluated and used in equation 1 to evaluate recrystallization (%) for intermediate stage.

$$\text{Recrystallization (\%)} = \frac{HV_{cold-rolled} - HV_{intermediate}}{HV_{cold-rolled} - HV_{fully\ recrystallized}} * 100\ \% \qquad (1)$$

Furthermore, grains with an aspect ratio of less than 2.6 were considered as recrystallized grains [36] and this area of recrystallized grains was used to evaluate the recrystallized fraction.

ImageJ software was used to evaluate the precipitate size and volume fraction. The precipitate shape was assumed to be circular in 2D and spherical in 3D. Area of precipitates were obtained after post-processing of STEM-EDS chemical maps in ImageJ software to determine size of precipitates (2*radius). Average thickness of FIB-lift out lamella was ~ 125 nm. Volume fraction of precipitates from an individual chemical map were evaluated using equation 2:

$$\text{Volume fraction of precipitates for the i}^{\text{th}} \text{ STEM-EDS chemical map} = \frac{\sum_{}^{4} \frac{4}{3}*\pi*radius^3}{thickness*area\ of\ i^{th}\ map} \qquad (2)$$

For quantitative analysis of average radius and volume fraction of precipitates, minimum of 600 precipitates were analysed from 15 different STEM-EDS chemical maps taken from two different FIB-lift out lamella.

2.4. Numerical prediction

Precipitate size and volume fraction in base and Ti+ grades were predicted for annealing temperature of 800 °C using MatCalc software, version 5.62.1004. Calculated precipitate size and volume fraction were used to evaluate Zener pinning force as described in discussion section 4.1. Parameters used for simulation of precipitation size and volume fraction are shown in Table 2.

Table 2 Parameters for MatCalc simulation of precipitate size and volume fraction

Type of precipitates	Diffusivity in ferrite (m²s⁻¹)	Interfacial energy	Critical energy for nucleation on dislocations
VC	$D_V^\alpha = 3.05 \times 10^{-4} \exp(-\frac{239000}{RT})$ [37]	0.445 [38]	0.01 [39]
TiC	$D_{Ti}^\alpha = 3.15 \times 10^{-4} \exp(-\frac{248000}{RT})$ [40]	0.425 [38]	0.01 [39]

For simulation, a start temperature of 600 °C was set and was gradually increased to 800 °C with increase over time (heating rate ~ 10 °C/s). Experimentally defined annealing conditions of 700 °C for 0 s, 800

°C for 0 s, 800 °C for 2 min and 800 °C for 5 min were equivalent to simulation time of 13 s, 25 s, 145 s and 325 s respectively. TCFE9 database in ThermoCalc software was utilised to evaluate equilibrium volume fraction of precipitates in the three grades for temperature range in between 500 °C to 1000 °C.

2.5. Mechanical testing

Wilson® VH3300 Automatic Hardness Tester was used to perform hardness measurements by carrying out 20 indents across the surface of cold-rolled and annealed samples. Load of 1000 g for dwell time of 10 s was applied during indentation. To evaluate mechanical properties such as yield, ultimate tensile strength and elongation, uniaxial tensile tests were performed using a 100 kN Schenck Trebel RM100 tensile testing machine at the Research & Development facilities of Tata Steel Europe. The crosshead was operated using force control with a constant loading rate of 30 MPa/s. To simulate annealing cold-rolled sheets of the three grades were annealed in a Continuous Annealing Simulator (CASim) for different conditions: 700 °C 0 s, 800 °C 0 s; 800 °C 2 min, 800 °C 5 min. Dog-bone shaped tensile samples of ISO/EM A50 size [41] were sectioned using water jet cutting from cold-rolled and annealed sheets. For each material condition, four tests were done for statistically reliable results.

3. Results

3.1. EBSD study of muffle furnace annealed samples

The as-received cold-rolled microstructure and texture of the base, Ti+ and Ti+Mn+ grades is very similar, with elongated grains usually defined as fibres [42]. These fibres are mainly dominated by the alpha (<110>//RD) and gamma (<111>//ND) fibres and minor portions of randomly oriented subgrains. The total amount of stored energy is assumed to be similar in all three steel grades because of the almost identical level of cold-rolled deformation (%) of ~ 70 % [43].

For an annealing temperature of 700 °C with no dwell, the nucleation of new ferrite grains is initiated along high angle grain boundaries for all three steel grades with insignificant change in microstructure as compared to cold-rolled state. For annealing condition of 800 °C 0 s, the base grade is almost fully recrystallized with the development of quasi-polygonal recrystallized grains (Fig. 2). Grain growth starts at the annealing temperature of 800 °C for dwell time of 15 min (Fig. 2) and continues with a massive grain growth for the dwell time of 2 h in the base grade.

For annealing at 800 °C for between 0 s to 30 min, recrystallization kinetics is slower in the Ti+ and Ti+Mn+ grades than in the base grade, with un-recrystallized ferrite matrix dominated by alpha fibre grains. {001}<110> grains of alpha fibre (shown as red coloured texture in ND-IPF EBSD maps of Fig. 2) have the lowest stored energy [44,45]. Therefore during annealing at the temperature of 800 °C for longer dwell time of 2 min to 30 min, {001}<110> grains have not fully recrystallized [46–49].

For the annealing condition of 800 °C 0 s, the microstructure of Ti+Mn+ grade is similar to that of the annealing condition of 700 °C 0 s with the nucleation of recrystallization occurring along the higher

angle grain boundaries. Fig. 3 shows a recrystallized grain nucleus along HAGB between alpha and gamma fibres (arrow marked as A) and between alpha and other random grain orientations (arrow marked as B) of Ti+Mn+ grade treated at 800 ℃ 0 s annealing condition. Areas of higher local misorientation form potential sites for nucleation of recrystallization such as deformation bands and HAGB between alpha/gamma texture [50,51].
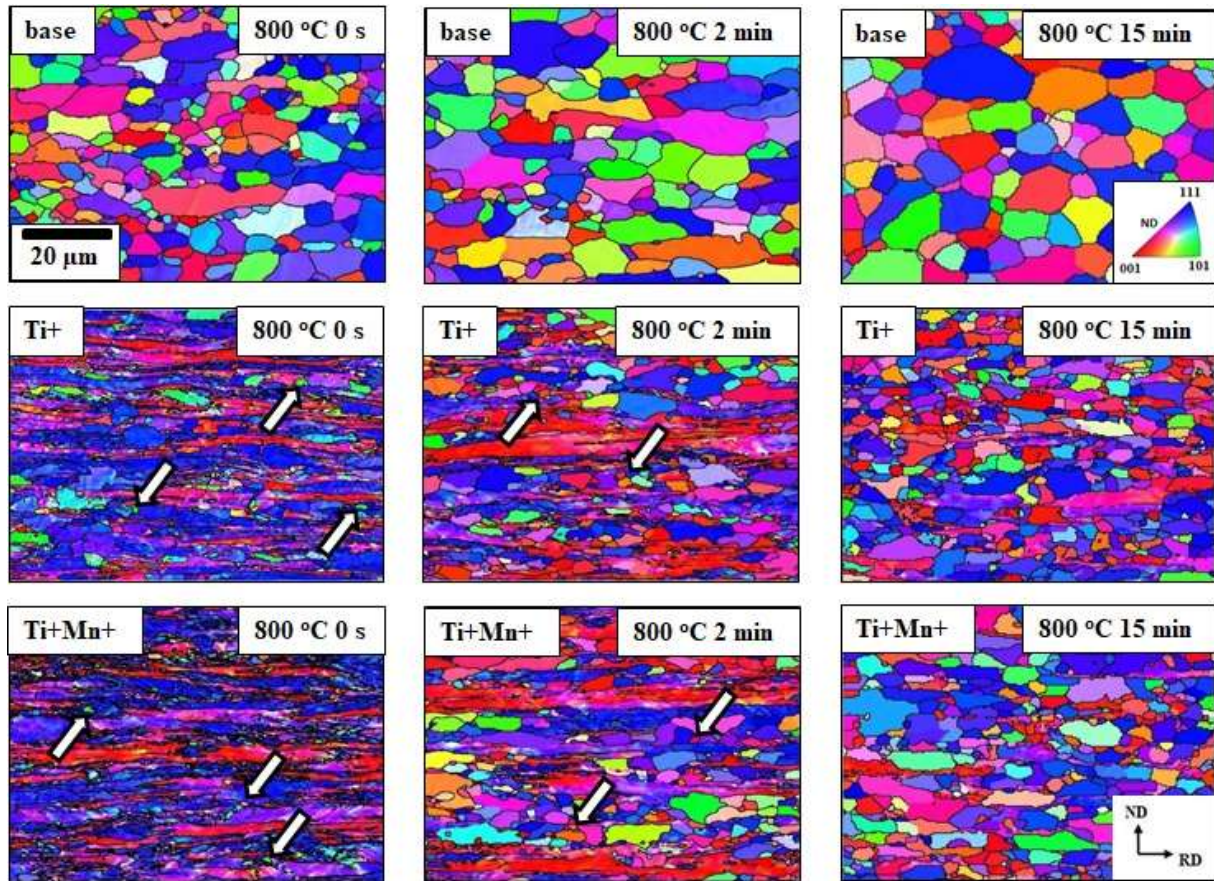

Fig. 2 Normal Direction Inverse Pole Figure (ND-IPF) maps of low-carbon microalloyed steel of base, Ti+ and Ti+Mn+ grades after annealing at 800 ℃ 0 s , 800 ℃ 2 min and 800 ℃ 15 min. Arrows indicate nucleation of recrystallized grains.

Maximum recrystallized grain size of the Ti+ and Ti+Mn+ grade is between 20 μm to 25 μm. While for the base grade, the relative frequency (%) of recrystallized grain (size > 30 μm) is greater than 10 %. For the annealing condition of 800 ℃ 2 h, average grain size of base grade (~ 50 μm) is much larger than Ti+ and Ti+Mn+ grades (~ 6 μm) as shown in Fig. 4.
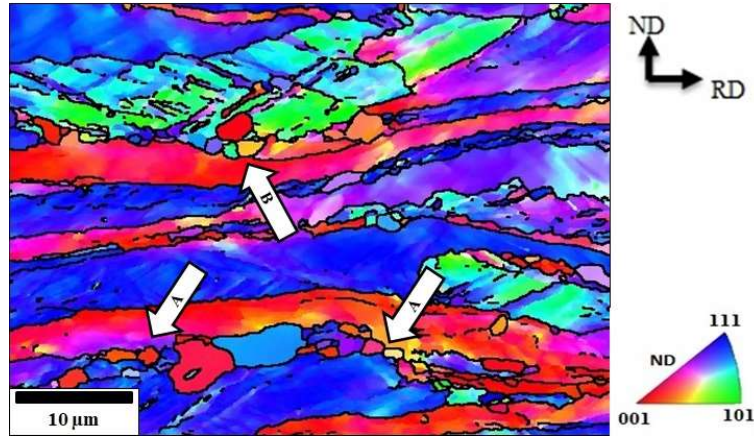
Fig. 3 Normal Direction Inverse Pole Figure (ND-IPF) map of low-carbon microalloyed steel of Ti+Mn+ grade after annealing at 800 °C 0 s at high magnification of x5k. Arrows 'A' and 'B' indicate nucleation of recrystallized grains along HAGB of alpha/gamma fibre and higher misorientation region between alpha fibre and random grain orientations respectively
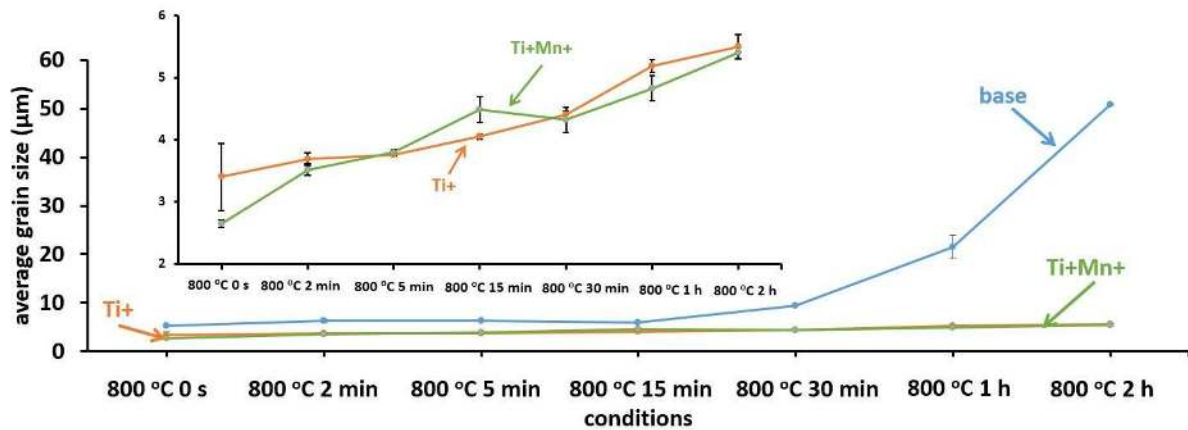

Fig. 4 Average grain size with aspect ratio > 2.6 of base, Ti+ and Ti+Mn+ grades (a) and Ti+ and Ti+Mn+ grades (b) for different annealing conditions: 800 °C 0 s; 800 °C 2 min; 800 °C 5 min; 800 °C 15 min; 800 °C 30 min; 800 °C 1 h and 800 °C 2 h

3.2. Evolution of Recrystallization (%)

Recrystallization (%) is evaluated by three methods: LAM, aspect ratio and hardness (HV/1) to quantitatively understand recrystallization behaviour among the three grades as shown in Fig. 5. Vickers hardness (HV/1) values of base, Ti+ and Ti+Mn+ grades for different conditions are presented in Fig. 7 and later discussed within the section 3.4. With increased annealing temperature and dwell time, recrystallization (%) is increased as shown in Fig. 5. For annealing condition of 800 °C 0 s: base grade is almost fully recrystallized and average recrystallization (%) of Ti+ grade (LAM method ~ 19 %) is slightly higher than Ti+Mn+ grade (LAM method ~ 8 %). With increase in dwell time (> = 2 min) at 800 °C, average recrystallization (%) of Ti+ and Ti+Mn+ are very similar as shown in Fig. 5.
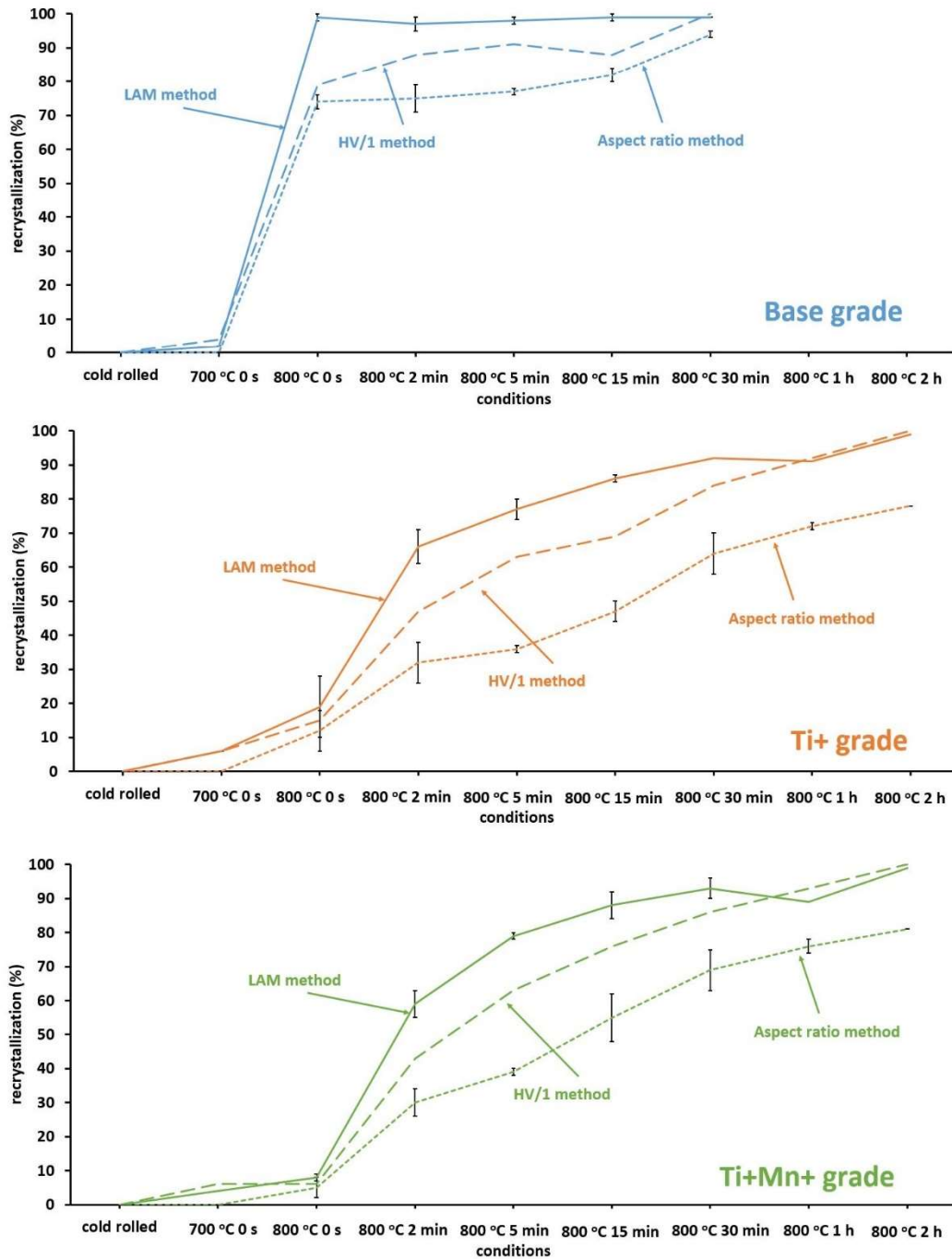
Fig. 5 Recrystallization (%) measurements using three different methods: local average misorientation (LAM), aspect ratio (AR) and Vickers hardness (HV/1) of base, Ti+ and Ti+Mn+ grades of steel for different conditions: cold-rolled; 700 ºC 0 s; 800 ºC 0 s; 800 ºC 2 min; 800 ºC 5 min; 800 ºC 15 min; 800 ºC 30 min; 800 ºC 1 h and 800 ºC 2 h

3.3. Evolution of precipitation during annealing

For the annealing condition of 700 ºC 0 s, fine precipitates of V(C/N) in base and (Ti,V)(C/N) in Ti+ and Ti+Mn+ grades are decorated along subgrain and grain boundaries of un-recrystallized ferrite matrix. Fine precipitates decorating the defects (Fig. 6a) provide resistance to the boundary motion by

Zener pinning during annealing [52]. Carbo-nitrides of Ti and V exist as complex precipitates due to their mutual solubility with each other in both Ti+ and Ti+Mn+ grades [53,54]. For higher temperature of 800 °C and dwell time of 2 min and 5 min (Fig. 6b), fine (d < 15 nm) and coarse (d > 15 nm) precipitates are present inside recrystallized ferrite grain of base, Ti+ and Ti+Mn+ grades.
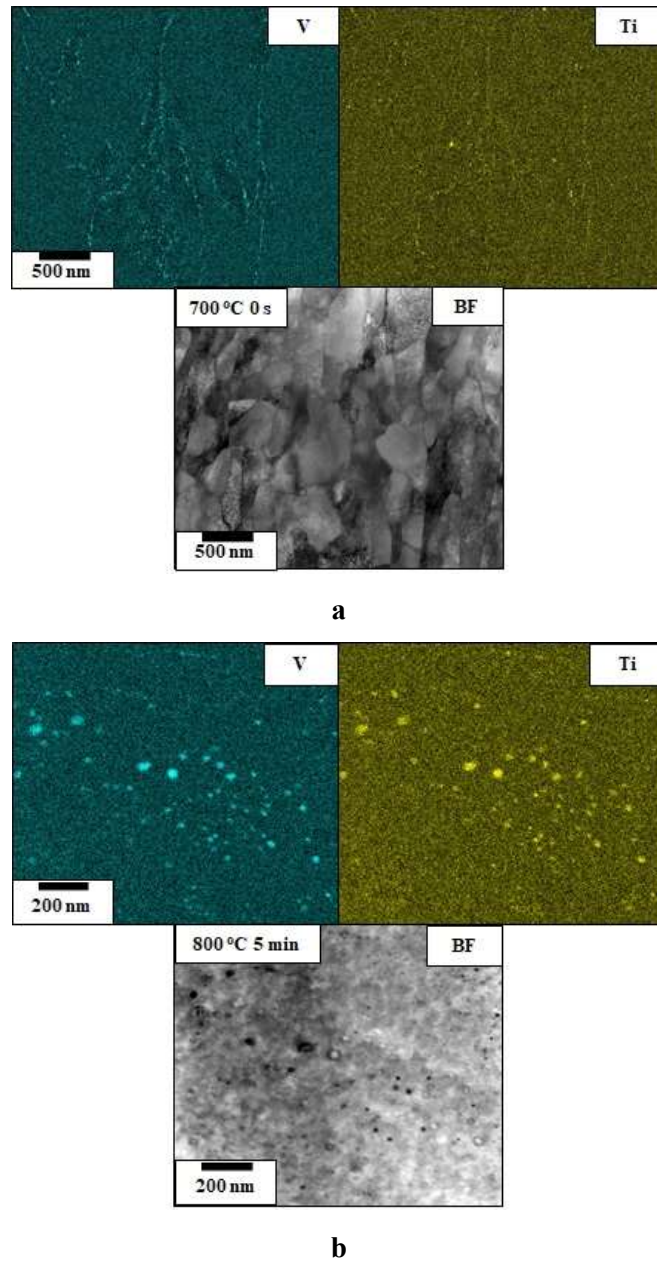

Fig. 6 STEM bright field (BF) image and EDS chemical maps of carbo-nitrides of carbo-nitrides of Titanium and Vanadium (Ti,V)C precipitates for Ti+Mn+ grade of steel annealed at 700 °C 0 s (a) and 800 °C 5 min (b) conditions at two different FIB-lift out samples for each grade after bulk-furnace annealing

Average precipitate size is increased with annealing temperature and dwell time for all three grades. For base grade, average precipitate size is coarser than Ti+ and Ti+Mn+ grades with increase in dwell time to 2 min and 5 min for annealing temperature of 800 °C as shown in Table 3.

Table 3: Precipitate size in base, Ti+ and Ti+Mn+ grades for annealing conditions of 700 °C 0 s, 800 °C 0 s, 800 °C 2 min and 800 °C 5 min

Grades	Precipitate size (nm) for different annealing conditions			
	700 °C 0 s	800 °C 0 s	800 °C 2 min	800 °C 5 min
Base	12.4 ± 1.7	13.1 ± 1.0	20.4 ± 7.7	21.4 ± 2.9
Ti+	11.2 ± 5.2	12.0 ± 5.5	13.6 ± 6.4	16 ± 2.4
Ti+Mn+	10.7 ± 4.1	13.6 ± 1.5	11.5 ± 1.1	14.3 ± 2.7

3.4. Hardness and uniaxial tensile measurements

Room temperature uniaxial tensile tests are performed to measure strength and elongation (%) properties of base, Ti+ and Ti+Mn+ grades treated for different conditions of as cold-rolled, and annealed at 700 °C 0 s, 800 °C 0 s, 800 °C 2 min and 800 °C 5 min. Proof strength (yield strength at 0.2 % strain), $R_{P0.2}$ is evaluated from the tensile curve and compared with empirical yield strength (YS) obtained from Vickers hardness (Fig. 7) using the relation (equation 3) as shown below [55]:

$$HV \sim 3 * YS \tag{3}$$

In equation 3, unit of Vickers hardness value is converted to MPa from kgf/mm^2 to evaluate empirical YS in MPa. There is insignificant difference between the empirical yield strength and $R_{P0.2}$ values of three grades for different conditions as shown in Fig. 8a. In cold-rolled state, average $R_{P0.2}$ and tensile strength (TS) of Ti+ ($R_{P0.2}$ = 946 ± 47 MPa and TS = 949 ± 44 MPa) and Ti+Mn+ ($R_{P0.2}$ = 1003 ± 2 MPa and TS = 1018 ± 8 MPa) grades are higher than base grade ($R_{P0.2}$ = 702 ± 8 MPa and TS = 719 ± 6 MPa). For annealing condition of 700 °C 0 s, strength values are similar to that of the cold-rolled state with elongation (%) (EL < 3 %). For the annealing temperature of 800 °C, $R_{P0.2}$ of the base grade significantly decreases to 350 - 390 MPa as shown in Fig. 8a, because of dislocation softening, recrystallization of deformed texture [56] and precipitate coarsening in recrystallized ferrite matrix. The elongation (%) of the base grade is increased up to 33 % for annealing condition of 800 °C 5 min as shown in Fig. 8c.

For annealing condition of 800 °C 0 s, $R_{P0.2}$ of Ti+ grade is decreased by approximately 100 MPa, which is more than Ti+Mn+ grade at about 20 MPa. With an increase in dwell time to 2 min for annealing temperature of 800 °C, TS of Ti+ and Ti+Mn+ grades have decreased to ~ 620 MPa. Elongation (%) of Ti+ and Ti+Mn+ grades is ~ 9 % as shown in Fig. 8c.
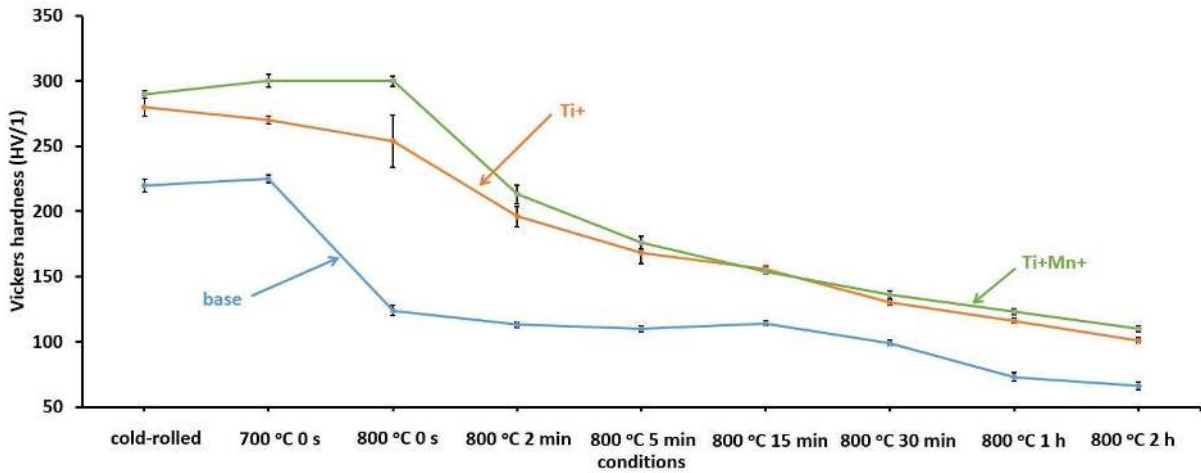
Fig. 7 Average Vickers hardness (HV/1) of base, Ti+ and Ti+Mn+ grades of steel for different conditions: 700 °C 0 s; 800 °C 0 s; 800 °C 2 min; 800 °C 5 min; 800 °C 15 min; 800 °C 30 min; 800 °C 1 h and 800 °C 2 h. In this plot, unit of Vickers hardness value is kgf/mm^2
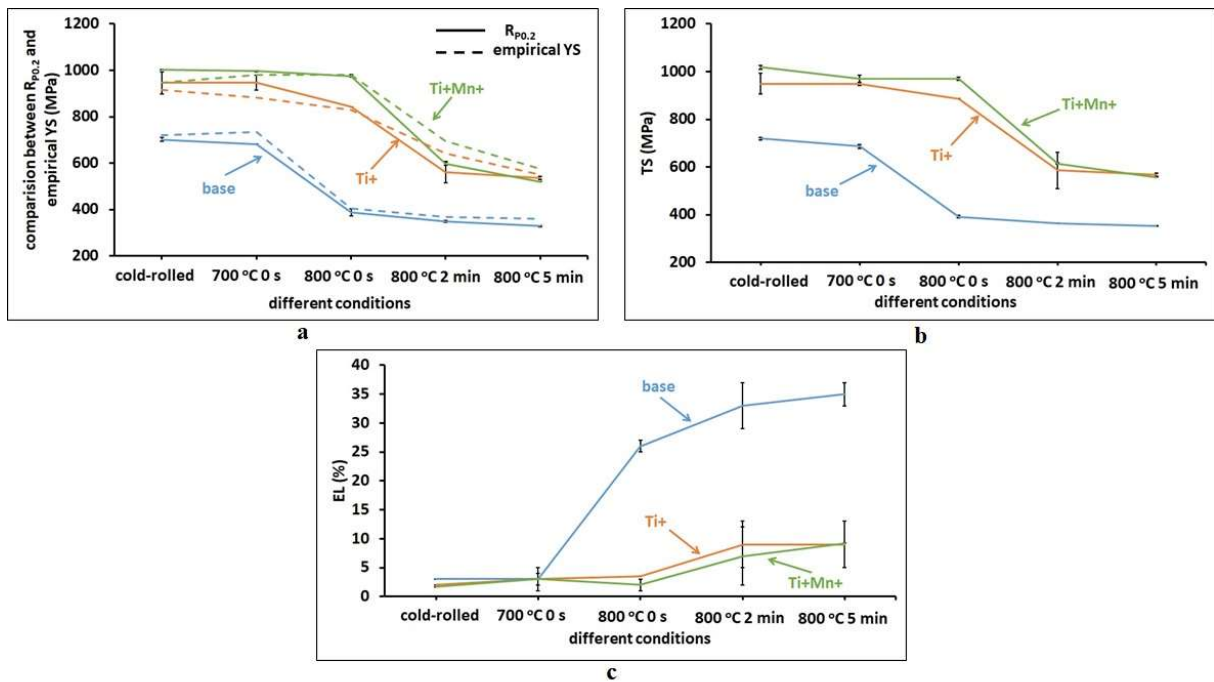

Fig. 8 Comparison of Yield strength at 0.2 % strain ($R_{P0.2}$) and empirical yield strength (YS) obtained from Vickers hardness (a), tensile strength (TS) (b) and elongation, EL (%) (c) of base, Ti+ and Ti+Mn+ grades of steel for different conditions: cold-rolled; 700 °C 0 s; 800 °C 0 s; 800 °C 2 min; 800 °C 5 min

4. Discussion

4.1. Initial precipitate state in the hot-rolled steel grades

Hot-rolled processing route (low simulated coiling temperature ~ 580 °C) and chemistry are designed in order to minimise the precipitation of vanadium and titanium carbides and also minimise the formation of iron-carbides in hot-rolled (as-received) microstructure [8,19,57–63]. STEM-EDS investigations of hot-rolled steel grades show fine (precipitate size, d < 5 nm) V(C/N) precipitates in

hot-rolled base grade and titanium rich (Ti,V)(C/N) precipitates in hot-rolled Ti+ and Ti+Mn+ grades are sparsely distributed along subgrain and grain boundaries (Fig. 9) and a small number of iron-carbide within ferrite matrix of hot-rolled Ti+ grade (Fig. 10). During annealing of cold-rolled steel grade, iron-carbide dissolves to release carbon back into ferrite matrix, as the alloy carbides are thermodynamically more stable than iron-carbides [64]. Upon further annealing, free C in ferrite phase combines with Ti and V to form precipitates in the cold-rolled and annealed steel grades.
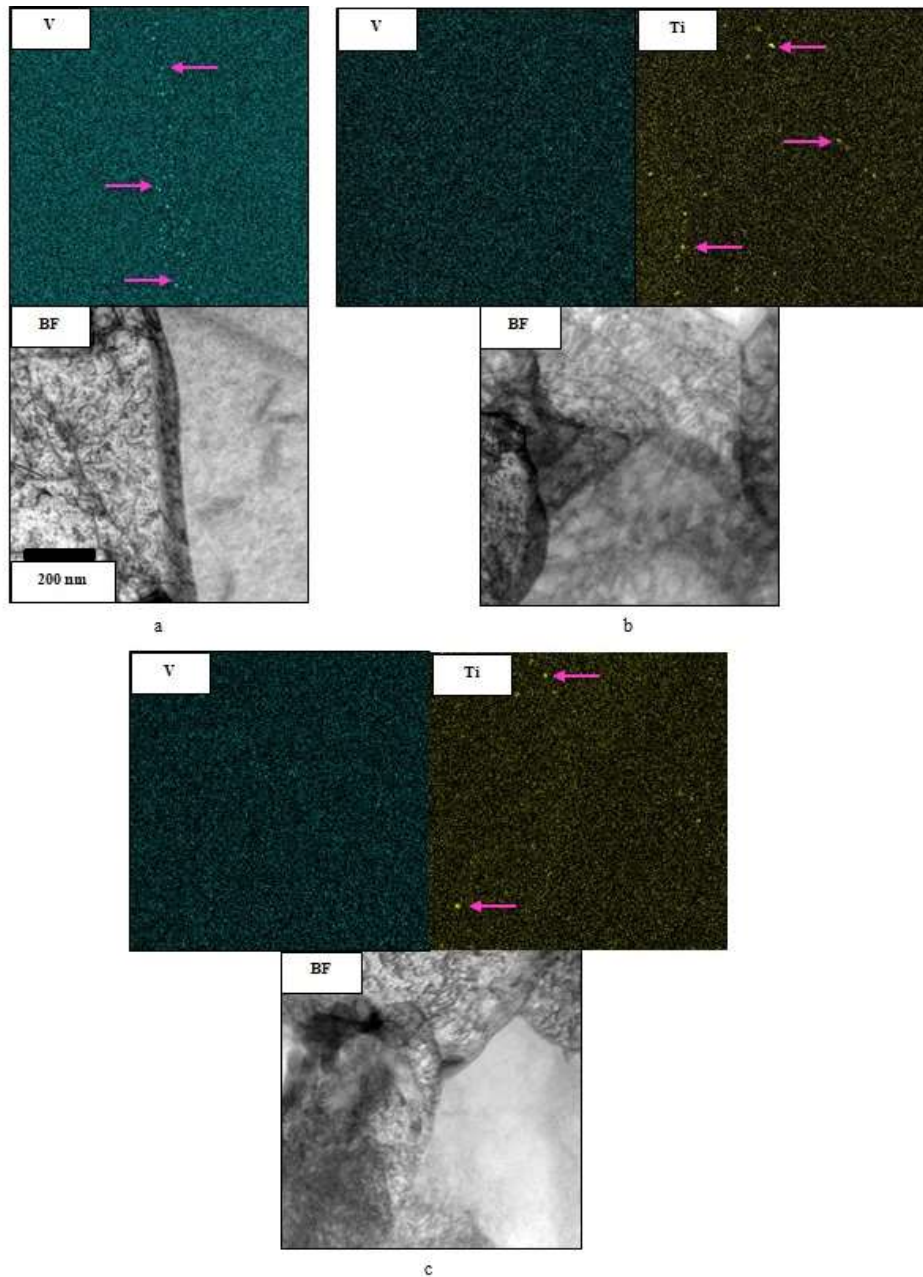

Fig. 9 STEM bright field (BF) image and EDS chemical maps of carbo-nitrides of Vanadium V(C/N) decorated along grain boundary and carbo-nitrides of Titanium and Vanadium (Ti,V)(C/N) present in ferrite matrix of hot-rolled condition of low-carbon microalloyed steel (as-received) of three different grades, base (a), Ti+ (b) and Ti+Mn+ (c). Arrows mark the precipitates present in ferrite matrix of hot-rolled base, Ti+ and Ti+Mn+ grades
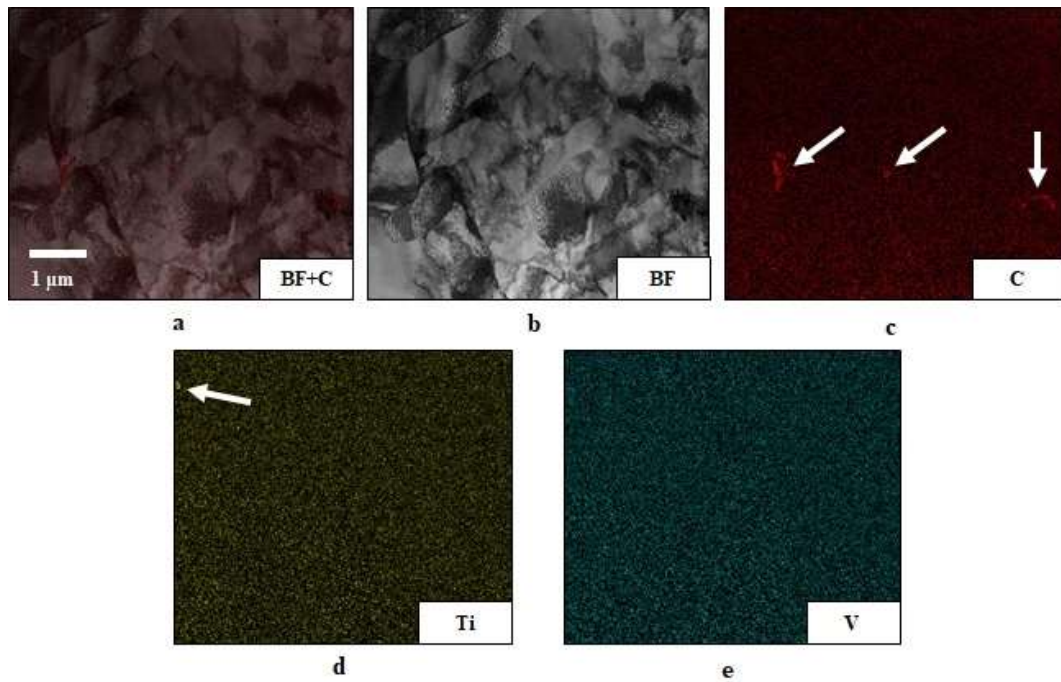
Fig. 10 STEM bright-field (BF) image superimposed with Carbon EDS chemical map (a) bright field (BF) image (b) and EDS chemical map of C (c), Ti (d) and V (e). Iron-carbide along subgrain boundary in the hot-rolled Ti+ grade. Arrows mark the iron-carbide in C chemical map and carbo-nitride of titanium in Ti chemical map

4.2. Competition between recrystallization and precipitation in base and Ti+ grades

Recrystallization and precipitation take place simultaneously and interact with each other in a complex form during annealing of microalloyed steel grades. On the one hand, precipitates interfere with dislocation and grain boundary movement and affect recovery and recrystallization kinetics, on the other hand, dislocations present in cold-rolled and annealed ferrite microstructure affect precipitation process [65]. Radius and volume fraction of precipitates are experimentally (from STEM-EDS maps) and numerically (from MatCalc simulation) determined and compared with each other for the base and Ti+ grades as shown in Fig. 11.

Experimental and numerical results of precipitate size and volume fraction are similar to each other for the annealing conditions of 800 °C 0 s, 800 °C 2 min and 800 °C 5 min as shown in Fig. 11a and 11b. For the annealing condition of 700 °C 0 s, experimental precipitate volume is higher than numerical predictions. For 700 °C 0 s, precipitates are very fine and closely spaced between each other along subgrain and grain boundaries. Quantification of precipitate size and volume fraction using ImageJ software may not be accurate and could result in different experimental and numerical observations.

MatCalc simulation estimates the critical radius of nucleation of precipitates in the Ti+ grade to be approximately 0.22 nm smaller than 4.2 nm in the base grade. The difference in critical radius of nucleation of precipitates is due to the difference in solubility of Ti and V in ferrite. The driving force for the formation of TiC particle is much higher than for VC because of the lower solubility of Ti in

ferrite matrix than that of V [66]. The higher driving force for nucleation promotes finer critical radius for nucleation of precipitates [39,67,68]. Driven by the higher force, the simulated precipitation kinetics is much faster in the Ti+ grade than in the base grade. For example, the precipitated volume fraction after 30 s annealing of Ti+ grade is about 0.15 %, which is much higher than the value (nearly zero or negligible) for the base grade. The faster precipitation kinetics in the Ti+ grade than in the base grade has a dramatic effect on the recrystallization kinetics in these two grades, as will be discussed next.

With increase in dwell time longer than 2 min at annealing temperature of 800 °C, precipitate coarsening occurs in the simulated radius curve of VC (base grade) due to the diffusion of solute atoms from the ferrite matrix [67]. The precipitate coarsening involves a growth of larger precipitates at the expense of smaller precipitates. However, the coarsening of TiVC (Ti+ grade) occurs at much later stage of annealing, i.e., after 1000 s (~ 15 min) annealing. Therefore, precipitate coarsening is easier to occur in the base than in the Ti+ grade during annealing at 800 °C as shown in Fig. 11. The above difference in the coarsening behaviour [67] is mainly due to the different composition of precipitates in these two grades. For the base grade, the precipitates are pure vanadium carbide (VC), however they are complex titanium vanadium carbides in the form of $Ti_yV_{1-y}C$ (average composition: $y \approx 0.4$, from MatCalc simulation) for the Ti+ grade. The above different coarsening behaviour also has a significant effect on recrystallization kinetics in these two grades.

Precipitate size and volume fraction are used in equation 4 to evaluate Zener pinning force (J/mol) for different annealing conditions:

$$\Delta G_{pin} = \frac{3}{2} * \sigma * N_v * \frac{f}{r} \qquad (4)$$

Where, f and r (in meters) are precipitate volume fraction and radius, and σ is interfacial energy of precipitates-ferrite matrix (value of 0.445 J/m^2 for VC [38] and 0.425 J/m^2 for TiC [38]), and N_v is molar volume (value of 7×10^{-6} m^3/mol). Fig. 10 shows numerical values of precipitate pinning force as a function of annealing time and corresponding ND-IPF EBSD maps of the base and Ti+ grades for the annealing condition of 800 °C 0 s, 800 °C 5 min, 800 °C 15 min and 800 °C 1 h.
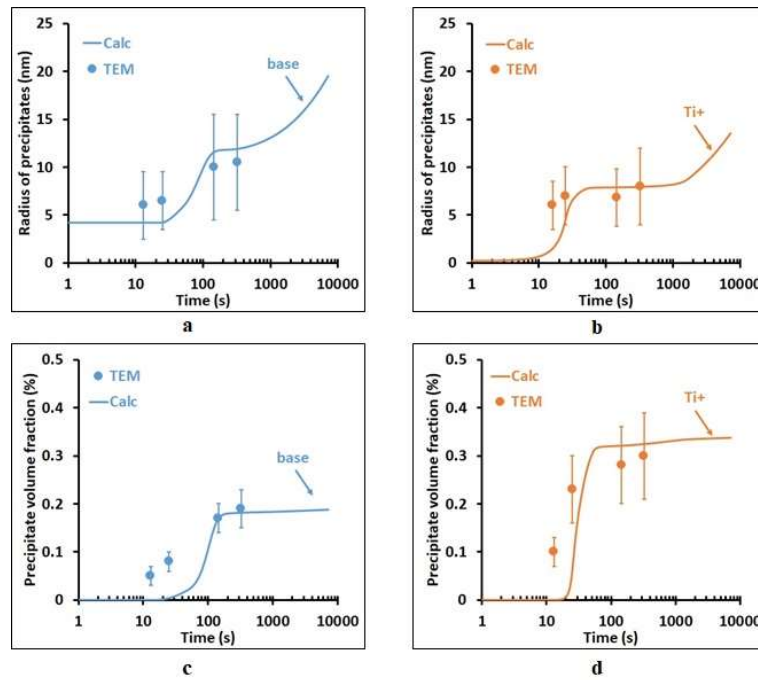
Fig. 11 Variation of experimentally evaluated (solid dot) and numerically evaluated, radius of precipitate and precipitate volume fraction (%) with increase in annealing time of the base (a, c) and the Ti+ (b, d) grades of steel. Annealing conditions: 700 °C 0 s, 800 °C 0 s, 800 °C 2 min and 800 °C 5 min correspond numerically to time: 13 s, 25 s, 145 s and 325 s respectively

For 800 °C 0 s, precipitation pinning force in the Ti+ grade of approximately 1 J/mol is much higher than in the base grade which is 0.06 J/mol as shown in Fig. 12. At this annealing time, the measured recrystallized fraction is about 100 % and 19 % in the base and Ti+ (Fig. 5) respectively. Comparing the above precipitation and recrystallization behaviour in these two grades, it's shown that the precipitation is faster than the recrystallization in the Ti+ grade, whilst the opposite situation happened in the base grade, i.e., the precipitation is much slower than the recrystallization. Once a lot of fine precipitates form in the Ti+ grade, the precipitation pinning force is effective in retarding recrystallization process in the Ti+ grade for the annealing condition of 800 °C 0 s. In the case of the base grade, lesser amount of precipitates is formed at this annealing condition and recrystallization is almost completed. Therefore, precipitation has negligible effect in retarding the recrystallization process in base grade. With an increase of dwell time to 2 min and to 5 min at 800 °C, recrystallization and precipitation occur concurrently in the Ti+ grade. The precipitation pinning force (about 1.75 Jmol^{-1}) could certainly be higher than the driving force for at least some grains belonging to alpha fibre with very low stored energy. For example, Dillamore et al. [44] measured stored energy of {001}<110> grain orientation of alpha fibre of cold-rolled steel ~ 1.70 Jmol^{-1} by TEM subgrain substructure analysis [44,69].This means that the recrystallization of those alpha grains is prevented temporally by the precipitates. Thus the presence of lower stored energy alpha fibre grains lead to a sluggish recrystallization process in the Ti+ grade.

With the increase in dwell time to 15 min or longer at 800 °C, the precipitate pinning force decreases (Fig. 12) in both base and Ti+ grades because of precipitate coarsening. When the pinning force decreases below the value of the driving force for recrystallization in the Ti+ grade, the recrystallization of those alpha grains with low stored energy could resume. For the base grade, because recrystallization is almost completed when the annealing temperature reaches 800 °C, the grain growth behaviour is affected by the precipitation coarsening in this grade. Some grains with much larger size (160 µm – 200 µm) than others (< 80 µm) could be observed for 1 and 2 hours annealing at 800 °C. From ND-IPF EBSD and STEM-EDS chemical maps it is observed that recrystallization and precipitation occur simultaneously in the base and Ti+ grades. For the base grade, precipitation is not significant enough to slow down recrystallization at 800 °C. While for the Ti+ grade, precipitation is significant enough to interfere with the grain boundary motion and result in sluggish recrystallization kinetics [63,70,71].
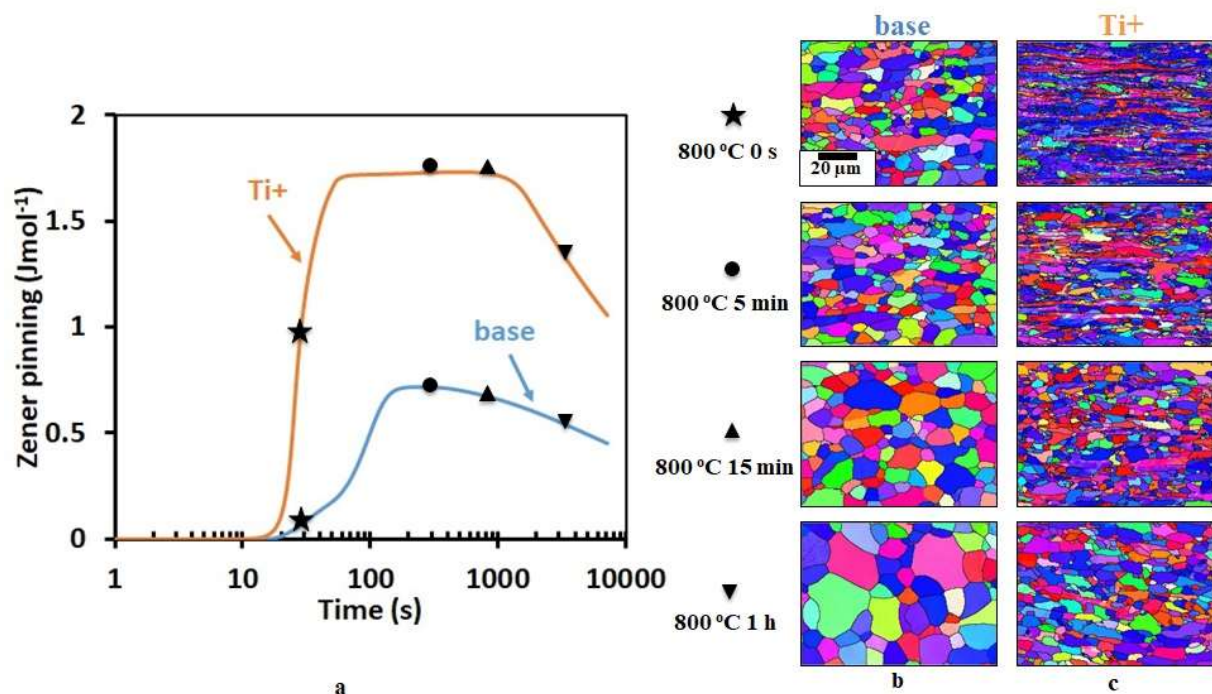

Fig. 12 Variation of numerically evaluated Zener pining force with increase in annealing time of the base and Ti+ grades of steel (a), ND-IPF maps of base (b) and Ti+ (c) grades for annealing condition of 800 °C 0 s, 800 °C 5 min, 800 °C 15 min and 800 °C 1 h . Annealing conditions: 800 °C 0 s, 800 °C 5 min, 800 °C 15 min and 800 °C 1 h correspond numerically to time: 25 s, 325 s, 925 s and 3625 s respectively

4.3. Effect of Mn solute drag on recrystallization process in Ti+Mn+ grade

The Ti+Mn+ grade has lower recrystallization (%) than the Ti+ grade at the annealing condition of 800 °C 0 s. For longer dwell times (> 0 s) at the annealing temperature of 800 °C, recrystallization behaviour of the Ti+ and Ti+Mn+ grades are similar. There is a difference in concentration of Mn solute atoms in the Ti+ grade (0.35 wt %) and the Ti+Mn+ grade (0.89 wt %). To understand in detail the significance of the solute drag (SD) of Mn and intrinsic boundary friction (IBF) [72] on retardation of recrystallization process, SD and IBF are plotted against the boundary velocity of the Ti+ and Ti+Mn+

grades as shown in Fig. 13. Solute drag force (ΔG_{sd}) and intrinsic boundary friction force (ΔG_{IBF}) are calculated using equations as shown below [72–74]:

$$\Delta G_{sd} = \frac{C_o * \alpha * v}{1 + \beta^2 * v^2} \tag{5}$$

$$\alpha = \frac{N_v * (k*T)^2 * \delta}{E_o * X} * \left(\sinh\left(\frac{E_o}{k*T}\right) - \left(\frac{E_o}{k*T}\right) \right) \tag{6}$$

$$\beta^2 = \frac{\alpha * k * T * \delta}{2 * N_v * E_o^2 * X} \tag{7}$$

$$\Delta G_{IBF} = \frac{v}{M_i} \tag{8}$$

$$M_i = \frac{2.63}{T} * e^{\left(\frac{-2075}{T}\right)} \tag{9}$$

Where, C_o is concentration of Mn solute atoms (0.0015 for the Ti+ grade and 0.0039 for the Ti+Mn+ grade), N_v is molar volume (value of 7×10^{-6} m³/mol), k is Boltzmann constant (value of 1.38×10^{-23} m²kgs⁻²K⁻¹), T is temperature (value of 1073 K), δ is grain boundary thickness (value of 5×10^{-10} m, assumed two times of Burgers vector of Fe lattice), E_o is grain boundary interaction energy with atoms (value of 1.7608×10^{-20} J/atoms), X is bulk diffusion constant (value of 0.000076*exp(-224400/R*T) m²/s), v is grain boundary velocity, and M_i is intrinsic grain boundary mobility [40,66,72–76].

Effective drag ($\Delta G_{sd} + \Delta G_{IBF}$) by Mn solute atoms is higher in the Ti+Mn+ grade than the Ti+ grade due to higher amount of Mn solutes. Recrystallization behaviour of both grades is sluggish, therefore velocity of grain boundary is considerably low (< 0.5 µm/s, see below for this estimation of growth speed). For the annealing condition of 800 °C 0 s, velocity of grain boundary is estimated using first order approximation [63] as explained below.

Nucleation for recrystallization starts at 700 °C 0 s in the Ti+ and Ti+Mn+ grades. Time to achieve the annealing temperature of 800 °C is ~ 15 s (recorded by data logger during bulk annealing experiment). Average recrystallized grain size at 800 °C 0 s of the Ti+ and Ti+Mn+ grades is 3.4 µm and 2.65 µm respectively. From a first order approximation value of the average grain boundary velocity (average grain size/time) of the Ti+ and Ti+Mn+ grades is ~ 0.23 µm/s and ~ 0.18 µm/s respectively. For a longer dwell time (> 0 s), the average grain boundary velocity would be theoretically lower than the above two values, considering the decreasing driving force due to recovery. From Mn solute drag versus boundary velocity plot in Fig. 13 it could be observed that the drag effect of Mn solute on boundary mobility for longer dwell time (> 0 s) is not significant in Ti+ and Ti+Mn+ grades due to the slow recrystallization speed (0.23 µm/s and 0.18 µm/s).

Apart from Mn solute drag effect on recrystallization, there could be other direct (for example, Mn-C dipole formation [77]) or indirect factors (for example, precipitation [66,78–83] or texture [84]) of Mn

solute atoms on recovery/recrystallization mechanism. Ushioda et al. [77] have studied the role of Mn in delaying the recovery during annealing, where dissolved C from cementite combines with Mn to form Mn-C complex. Mn-C complex or Mn-C dipole is formed by interaction (attractive) between Mn substitutional atoms and C interstitial atoms [85–88]. Interaction between Mn substitutional atom and C interstitial atom is originated from the elastic-strain field around Mn substitutional atom in BCC Fe lattice [88,89]. Mn-C complex interfere with dislocation movement during recovery and leads to a delay in the incubation time for recrystallization, i.e. nucleation of recrystallization is delayed.
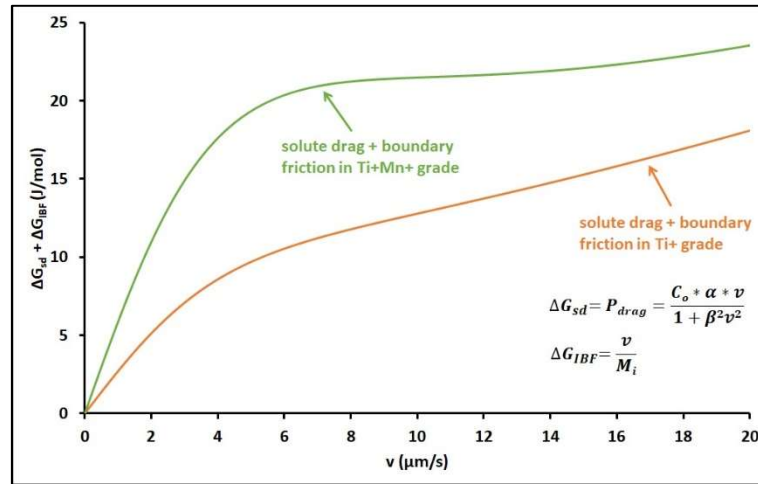

Fig. 13 Variation of effective drag i.e. combined solute drag (SD) and intrinsic boundary friction (IBF) with increase in grain boundary velocity during annealing for the Ti+ and Ti+Mn+ grades of steel

Mn also affects precipitation kinetics in the austenite phase. It is proposed that higher amount of Mn solutes increases the solubility of TiC precipitate in austenite phase [82,83] and delays precipitation kinetics. The effect of Mn solute content on precipitation kinetics in the austenite phase is well known [66,78–83], however there are not any conclusive data published on the Mn solute content effect on the precipitate solubility in the ferrite phase. The equilibrium precipitate volume fraction is plotted for the three grades for equilibrium state as shown in Fig. 14. There is negligible effect of Mn solute content on precipitation thermodynamics in ferrite phase of the Ti+ and Ti+Mn+ steel grades, when temperature is lower than 750 °C. Mn could indirectly influence precipitation kinetics by segregating along dislocations and interfere with precipitation process in ferrite [77,81]. Moreover it is known that {001}<110> grains of alpha fibre have lower stored energy than {112}<110> grains of alpha fibre [45,47]. Therefore, the difference in maximum peak of texture intensity in the cold-rolled state (Fig. 15) could also result in a slower recrystallization kinetics in the Ti+Mn+ grade than in the Ti+ grade for the annealing condition of 800 °C 0 s.
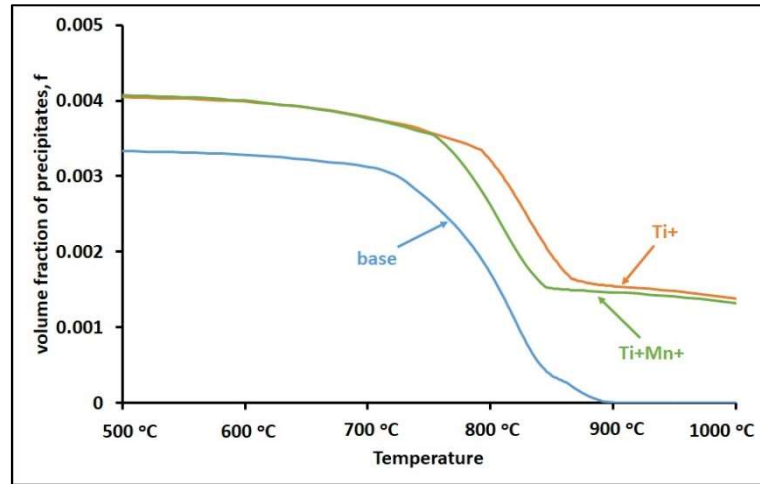
Fig. 14 Variation of volume fraction of precipitates with increase in temperature 500 °C to 1000 °C for the base, Ti+ and Ti+Mn+ grades of steel in equilibrium condition evaluated from ThermoCalc using TCFE9 database
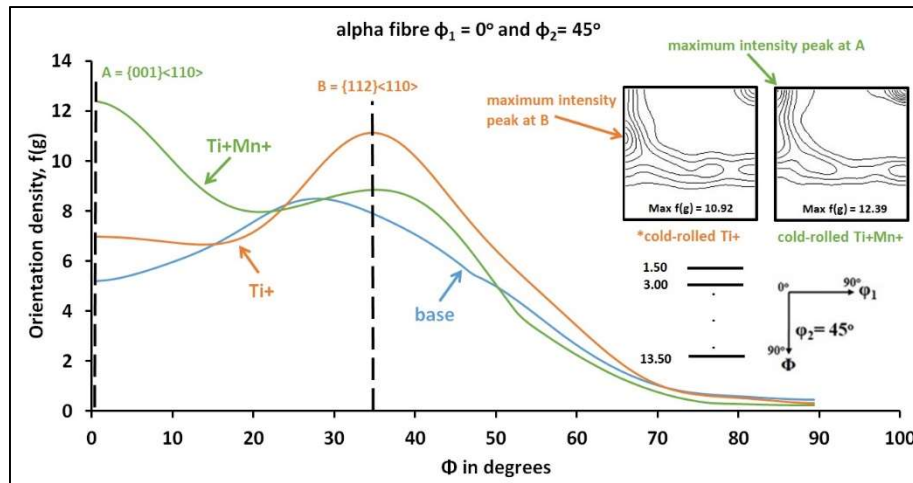

Fig. 15 Variation in orientation density of alpha fibre grains with increase in Φ from 0° to 90° for constant φ₂ = 45° for the cold-rolled low-carbon microalloyed steel of base, Ti+ and Ti+Mn+ grades. 2D ODF maps of cold-rolled Ti+ and Ti+Mn+ grades show maximum intensity peak around grain orientation {112}<110> and {001}<110> respectively (*cold-rolled Ti+ grade texture [32]).

4.4. Combined strength evaluation for the base, Ti+ and Ti+Mn+ grades for the annealing condition of 800 °C 2 min

Strengthening contribution from dislocation density, grain size, inherent ferrite matrix, precipitate and solid solution of the base, Ti+ and Ti+Mn+ grades is evaluated for the annealing condition of 800 °C 2 min. The empirical relation to evaluate combined strength comprising of solid solution strength, inherent strength of matrix and grain refinement strength of ferritic microalloyed steel is given by Pickering et al. [90,91] (Equation 10):

$$\sigma_y \text{(MPa)} = 15.4(3.5 + 2.1[\%Mn] + 5.4[\%Si] + 23[\%N] + 1.13d^{-0.5}) \qquad (10)$$

Where [%Mn], [%Si] and [%N] are the weight (%) of manganese, silicon and nitrogen in ferrite solution respectively and d is the average ferrite grain size in mm. For this study, free carbon and nitrogen are assumed to be negligible in the solid solution and are taken in combination with titanium and vanadium as carbides and nitrides for the annealing condition of 800 °C 2 min.

Average dislocation density is equated to average GND [92,93] to evaluate dislocation strengthening [94]:

$$\sigma_d = \alpha M \mu b \rho^{0.5} \qquad (11)$$

Where α is a constant, M is average Taylor factor, μ is shear modulus, b is magnitude of the Burger's vector and ρ is dislocation density. Typical values for Fe ($\alpha \sim 0.3$, $M \sim 3$, $\mu \sim 75$ GPa and $b \sim 0.25$ nm) [94] are used in equation 9. Average GND density of the base, Ti+ and Ti+Mn+ grades are $\sim 1.00E+13$ m^{-2}, $1.05E+14$ m^{-2} and $1.15E+14$ m^{-2} respectively estimated from LAM maps obtained from Channel 5 software of Oxford Instruments [32].

Precipitation strengthening is evaluated using Ashby-Orowan equation [66]:

$$\sigma_p = 10.8 \frac{\sqrt{f}}{d} \ln \frac{d}{6.125 x 10^{-4}} \qquad (12)$$

Where f and d are average volume fraction and size of precipitate. Average volume fraction of precipitates of the base, Ti+ and Ti+Mn+ grades for the annealing condition of 800 °C 2 min are $\sim$ 0.002, $\sim$ 0.003 and $\sim$ 0.002 respectively. Solid solution strength, inherent strength of matrix, grain refinement strength, dislocation density strength and precipitation strength are added together to evaluate effective yield strength and compared with yield strength ($R_{P0.2}$) from the tensile test of different grades as shown in Fig. 16.

Grain size strengthening is dominant for the base, Ti+ and Ti+Mn+ grades of steel. High dislocation density ($\sim 10^{14}$ m^{-2}) in un-recrystallized ferrite matrix and fine precipitates lead to a higher yield strength (200 MPa to 250 MPa) of the Ti+ and Ti+Mn+ grades than of the base grade. Effective yield strength is about 16 % to 20 % higher than yield strength from the tensile test as shown in Fig. 16. For the grain size strengthening calculation, average recrystallized grain size is used in equation 10. Partially recrystallized matrix is a mixture of un-recrystallized elongated grains and quasi-polygonal recrystallized grains. It is assumed that the average grain size of the partially recrystallized sample is equal to average recrystallized grain size [62] and could result in an overestimation of the grain size strengthening contribution. Higher contribution from grain size strengthening could further result in a higher effective yield strength value than the yield strength obtained from the tensile test.
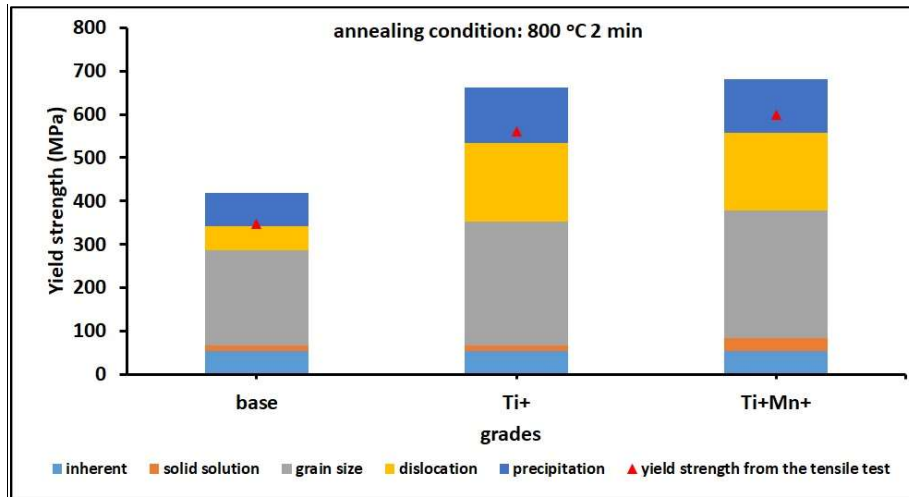
Fig. 16 Effective yield strength (combination of inherent, solid solution, grain size, dislocation, precipitation strength) and yield strength from the tensile test for the base, Ti+ and Ti+Mn+ grades of steel for the annealing condition of 800 °C 2 min

The strengthening contribution from precipitation in the base grade is lower than the other two grades for the annealing condition of 800 °C 2 min. Coarser average precipitate size and lower average volume fraction of V(C/N) in the base grade (~ 20 nm and 0.002) than (Ti/V)(C/N) in the Ti+ grade (~ 14 nm and 0.003) lead to lower precipitation strengthening in the base grade (Fig. 17). Similarly, a high volume fraction of very fine precipitates (~ 3 nm) in the Nb-V-Mo [8] and Ti-Mo [30] commercial hot-rolled steel products of Tata Steel Europe [8] and JFE Steel Corporations respectively [30] leads to higher precipitation strengthening of around 400 MPa to 500 MPa. During phase transformation from austenite to ferrite, precipitates nucleate along dislocations, subgrain/grain boundaries and at the austenite to ferrite moving interphase [76]. By controlling the coiling temperature and the sample chemistry, very fine (~ 5 nm) rows of interphase precipitates are developed to provide high precipitation strengthening [8,19]. During sub-critical annealing of cold-rolled low-carbon microalloyed steel, precipitates nucleate along dislocations and subgrain/grain boundaries. Controlling the dwell time of sub-critical annealing cycle to simultaneously obtain fine recrystallized grain and fine precipitates is challenging. Annealing time required to achieve fine fully recrystallized grains in cold-rolled annealed steel could lead to precipitate coarsening and dislocation annihilation [27].

From the results and discussions it could be found that the correlative material characterisation technique of EBSD and FIB-lift out STEM is a significant tool for studying recrystallization and precipitation evolution and their interactions during sub-critical annealing of cold-rolled microalloyed steel. Experimental observations of EBSD and STEM and numerical predictions of MatCalc software give a clear understanding of the fast recrystallization kinetics and precipitates coarsening in base grade and sluggish recrystallization kinetics in Ti+ and Ti+Mn+ grades. Additional investigation to further increase the strength to elongation balance, such as through application of intercritical annealing to

generate very fine interphase and random precipitates in the soft ferrite phase is currently in progress and will be published separately.
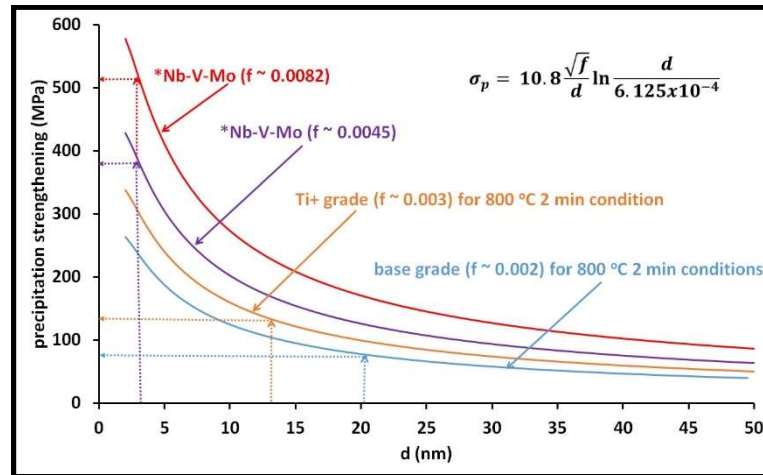

Fig. 17 Variation of the precipitation strengthening as a function of the precipitate size from 0 nm to 50 nm for base and Ti+ steel cold-rolled and annealed at 800 °C 2 min and for *Tata Steel commercial hot-rolled Nb-V-Mo grades of steel [8]. Notation 'f' stands for volume fraction of precipitates

5. Conclusions

- Recrystallization kinetics is much faster in the base grade as compared to the Ti+ and Ti+Mn+ grades. Presence of additional Ti-microalloying element along with V in the Ti+ and Ti+Mn+ grades is effective in retarding the recrystallization process during sub-critical annealing.

- Higher intensity of {001}<110> grain orientation and additional Mn solute atoms in the Ti+Mn+ grade leads to a slower recovery rate as compared to the base and Ti+ grades under the annealing condition of 800 °C 0 s.

- There is insignificant difference observed in recrystallization kinetics between the Ti+ and Ti+Mn+ grades for longer dwell time (> 0 s) at the annealing temperature of 800 °C. The solute drag effect by additional Mn solute atoms on recrystallization kinetics of the Ti+Mn+ grade is negligible due to sluggish subgrain/grain boundary movement.

- Coarsening of precipitates during sub-critical annealing of the base, Ti+ and Ti+Mn+ grades leads to lower precipitation strengthening as compared to Nb-V-Mo [8] and Ti-Mo [30] commercial hot-rolled steel grades, where higher precipitation strengthening is achieved by very fine (~ 3 nm) interphase precipitation.

- Precipitation pinning potential is higher for the Ti+ grade than for base grade due to the presence of additional Ti-microalloying element along with V in the Ti+ grade. The strong pinning potential results in sluggish recrystallization behaviour in the Ti+ grade. But the precipitation in the base grade is slower than recrystallization, and thus has no or negligible pinning effect on recrystallization.

Acknowledgements

Data availability

The raw/processed data required to reproduce these findings cannot be shared at this time due to technical or time limitations.

References

[1]   J.M. Allwood, J.M. Cullen, M.A. Carruth, Sustainable Materials with Both Eyes Open, UIT Cambridge Limited, 2012.

[2]   R. Rana, S.B. Singh, Automotive Steels: Design, Metallurgy, Processing and Applications, Elsevier Science, 2016.

[3]   2017 UK greenhouse gas emissions: provisional figures - statistical release, 2018.

[4]   Business Energy and Industrial Strategy Comittee, Electric vehicles: driving the transition, House of Commons. (2018) 6. https://publications.parliament.uk/pa/cm201719/cmselect/cmbeis/383/383.pdf.

[5]   A. Arankalle, Advances in Light Weight Materials for Body-in-White (BIW), in: Innov. Des. Dev. Pract. Aerosp. Automot. Eng., Springer, 2017: pp. 517–525.

[6]   R. Grimes, R. Dashwood, H. Flower, Processing of high superplastic strain rate aluminium alloys, Alum. Int. Today. 15 (2003) 64.

[7]   I. Kapoor, R.G. Narayanan, S. Taylor, V. Janik, R. Dashwood, Predicting the Warm Forming Behavior of WE43 and AA5086 Alloys, in: Procedia Eng., 2017: pp. 897–904. https://doi.org/10.1016/j.proeng.2016.12.136.

[8]   R.A. Rijkenberg, A. Blowey, P. Bellina, C. Wooffindin, Advanced High Stretch-Flange Formability Steels for Chassis & Suspension Applications 3 . Product concept : tensile properties and microstructure, in: 4th Int. Conf. Steels Cars Truck. June 15-19, Braunschweig, Ger., 2014: pp. 426–433.

[9]   H. Adam, Carbon fibre in automotive applications, Mater. Des. 18 (1997) 349–355. https://doi.org/10.1016/S0261-3069(97)00076-9.

[10]   T. Sakayama, G. Murayma, Y. Naito, K. Saita, Y. Miyazakki, H. Oikawa, T. Nose, similar metal joining technologies for steel sheet and aluminum alloy sheet in auto body, 2012. https://doi.org/C 621 . 791 / . 792 : 621 . 88 : 669 . 14 - 415 : 669 . 715 : 629 . 11 . 011 . 5.

[11]   P.K. Mallick, Materials, Design and Manufacturing for Lightweight Vehicles, CRC press, Boca Raton, 2010. https://doi.org/10.1533/9781845697822.2.309.

[12]   N. Baluch, Z.M. Udin, C.S. Abdullah, Advanced high strength steel in auto industry: an overview, Eng. Technol. Appl. Sci. Res. 4 (2014) 686–689.

[13]   R. Kuziak, R. Kawalla, S. Waengler, Advanced high strength steels for automotive industry, Arch. Civ. Mech. Eng. 8 (2008) 103–117. https://doi.org/https://doi.org/10.1016/S1644-9665(12)60197-6.

[14]   N. Gope, D.K. Rout, S. Mukherjee, G. Jha, A.N. Bhagat, A.K. Verma, D. Bhattarjee, High strength steels for automotive applications: Recent trends and experience at tata steel, SAE Trans. 26 (2005) 333–344.

[15]   T. Nanda, V. Singh, V. Singh, Third generation of advanced high-strength steels : Processing

routes and properties, in: Proc. Inst. Mech. Eng. Part L J. Mater. Des. Appl., 2016: pp. 1–30. https://doi.org/10.1177/1464420716664198.

[16] K. Takashima, K. Hasegawa, Y. Toji, Y. Funakawa, Void generation in cold-rolled dual-phase steel sheet having excellent stretch flange formability, ISIJ Int. 57 (2017) 1289–1294. https://doi.org/10.2355/isijinternational.ISIJINT-2017-086.

[17] K. Hasegawa, K. Kawamura, T. Urabe, Y. Hosoya, Effects of microstructure on stretch-flange-formability of 980 MPa grade cold-rolled ultra high strength steel sheets, ISIJ Int. 44 (2004) 603–609. https://doi.org/10.2355/isijinternational.44.603.

[18] P.B. Lake, J.J. Grenawalt, Partially Annealed High Strength Cold Rolled Steels, SAE Trans. (1977). https://doi.org/10.4271/770163.

[19] Y. Funakawa, T. Shiozaki, K. Tomita, T. Yamamoto, E. Maeda, Development of High Strength Hot-rolled Sheet Steel Consisting of Ferrite and Nanometer-sized Carbides, ISIJ Int. 44 (2004) 1945–1951. https://doi.org/10.2355/isijinternational.44.1945.

[20] T. Inoue, S. Kinoshita, Initiation of ductile fracture voids in a spheroidized stee, J. JSTP. 14 (1973) 291.

[21] H. long YI, L. xiu DU, G. dong WANG, X. hua LIU, Strengthening Mechanism of a New 700 MPa Hot Rolled High Strength Steel, J. Iron Steel Res. Int. 15 (2008) 76–80. https://doi.org/10.1016/S1006-706X(08)60036-9.

[22] Z. Liu, R.O. Olivares, Y. Lei, C.I. Garcia, G. Wang, Microstructural characterization and recrystallization kinetics modeling of annealing cold-rolled vanadium microalloyed HSLA steels, J. Alloys Compd. 679 (2016) 293–301. https://doi.org/10.1016/j.jallcom.2016.04.057.

[23] M. Janošec, I. Schindler, V. Vodárek, J. Palát, S. Rusz, P. Suchánek, M. Rüžička, E. Místecký, Microstructure and mechanical properties of cold rolled, annealed HSLA strip steels, Arch. Civ. Mech. Eng. 7 (2007) 29–38. https://doi.org/https://doi.org/10.1016/S1644-9665(12)60208-8.

[24] W. Bleck, Cold-rolled, high-strength sheet steels for auto applications, Jom. 48 (1996) 26–30. https://doi.org/10.1007/BF03222991.

[25] N. Prasad, S. Kumar, P. Kumar, S.N. Ojha, Mechanical properties of a cold-rolled annealed HSLA steel, J. Mater. Sci. 26 (1991) 5158–5162. https://doi.org/10.1007/BF01143207.

[26] T. Matsuoka, K. Yamamori, Metallurgical aspects in cold rolled high strength steel sheets, Metall. Trans. A. 6 (1975) 1613–1622. https://doi.org/10.1007/BF02641975.

[27] J. Raines, D. Matlock, J.G. Speer, R. Glodowski, Influence of V(C,N)precipitation potential on recovery annealing response of microalloyed sheet steel, Iron Steel Technol. 8 (2011) 109–116.

[28] Tata, Strip products and services catalogue 2018, (2018).

[29] K. Yoshida, Present and Future Status of High Strength Steel Sheets for Japanese Autobodies., Trans. Iron Steel Inst. Japan. 21 (1981) 761–766. https://doi.org/10.2355/isijinternational1966.21.761.

[30] K. Seto, Y. Funakawa, S. Kaneko, Hot rolled high strength steels for suspension and chassis parts "NANOHITEN" and "BHT® Steel," JFE Tech Rep. 10 (2007) 19–25.

[31] EBSD - Electron Backscatter Diffraction, Oxford Instruments. (2017). https://www.oxford-instruments.com/products/microanalysis/ebsd (accessed April 27, 2017).

[32] I. Kapoor, Y. Lan, A. Rijkenberg, Z. Li, V. Janik, Quasi in-situ analysis of geometrically necessary dislocation density in α-fibre and γ-fibre during static recrystallization in cold-rolled low-carbon Ti-V bearing microalloyed steel, Mater. Charact. 145 (2018) 686–696. https://doi.org/10.1016/j.matchar.2018.09.032.

[33] C. Moussa, M. Bernacki, R. Besnard, N. Bozzolo, About quantitative EBSD analysis of deformation and recovery substructures in pure Tantalum, IOP Conf. Ser. Mater. Sci. Eng. 89 (2015). https://doi.org/10.1088/1757-899X/89/1/012038.

[34] M. Calcagnotto, D. Ponge, E. Demir, D. Raabe, Orientation gradients and geometrically necessary dislocations in ultrafine grained dual-phase steels studied by 2D and 3D EBSD, Mater. Sci. Eng. A. 527 (2010) 2738–2746. https://doi.org/10.1016/j.msea.2010.01.004.

[35] T. Ogawa, N. Maruyama, N. Sugiura, N. Yoshinaga, Incomplete recrystallization and subsequent microstructural evolution during intercritical annealing in cold-rolled low carbon steels, ISIJ Int. 50 (2010) 469–475. https://doi.org/10.2355/isijinternational.50.469.

[36]   C. Wu, H. Yang, H.W. Li, Simulated and experimental investigation on discontinuous dynamic recrystallization of a near-α TA15 titanium alloy during isothermal hot compression in β single-phase field, Trans. Nonferrous Met. Soc. China (English Ed. 24 (2014) 1819–1829. https://doi.org/10.1016/S1003-6326(14)63259-3.

[37]   S. Yamasaki, H.K.D.H. Bhadeshia, Modelling and characterisation of V4C3 precipitation and cementite dissolution during tempering of Fe - C - V martensitic steel, Mater. Sci. Technol. 19 (2003) 1335–1343. https://doi.org/10.1179/026708303225005971.

[38]   J.H. Jang, The Effect of Mo or W on TiC Coarsening in HSLA Steel, Pohang University of Science and Technology, 2012.

[39]   F. Perrard, A. Deschamps, P. Maugis, Modelling the precipitation of NbC on dislocations in α-Fe, Acta Mater. 55 (2007) 1255–1266. https://doi.org/10.1016/j.actamat.2006.10.003.

[40]   K. Xu, Multiphase particle-size-grouping model of precipitation and its application to thermal processing of microalloyed steel, University of Illinois at Urbana-Champaign, 2012.

[41]   D.N. Hanlon, S.M.C. van Bohemen, S. Celotto, Critical Assessment 10: Tensile elongation of strong automotive steels as function of testpiece geometry, Mater. Sci. Technol. 31 (2015) 385–388. https://doi.org/10.1179/1743284714Y.0000000707.

[42]   O. Engler, V. Randle, Chapter 1 - Introduction, in: Introd. to Texture Anal. Macrotexture, Microtexture, Orientat. Mapp., Second, CRC press, Boca Raton, 2009: pp. 3–14.

[43]   C. Fang, Annealing and Precipitation Behavior During Batch Annealing of HSLA Steels, University of Science and Technology Beijing, 2000.

[44]   I.L. Dillamore, C.J.E. Smith, T.W. Watson, Oriented Nucleation in the Formation of Annealing Textures in Iron, Met. Sci. J. 1 (1967) 49–54. https://doi.org/10.1179/msc.1967.1.1.49.

[45]   I. Thomas, S. Zaefferer, F. Friedel, D. Raabe, High-Resolution EBSD Investigation of Deformed and Partially Recrystallized IF Steel, Adv. Eng. Mater. 5 (2003) 566–570. https://doi.org/10.1002/adem.200300373.

[46]   A. Belyakov, F.G. Wei, K. Tsuzaki, Y. Kimura, Y. Mishima, Incomplete recrystallization in cold worked steel containing TiC, Mater. Sci. Eng. A. 471 (2007) 50–56. https://doi.org/10.1016/j.msea.2007.04.022.

[47]   I.L. Dillamore, J.G. Roberts, A.C. Bush, Occurrence of shear bands in heavily rolled cubic metals, Met. Sci. 13 (1979) 73–77. https://doi.org/10.1179/msc.1979.13.2.73.

[48]   J.L. Bocos, E. Novillo, M.M. Petite, A. Iza-Mendia, I. Gutierrez, Aspects of orientation-dependent grain growth in extra-low carbon and interstitial-free steels during continuous annealing, Metall. Mater. Trans. A. 34 (2003) 827. https://doi.org/10.1007/s11661-003-0117-x.

[49]   D. Zhuang, L. Wang, Y. Huang, X. Li, H. Zhang, D. Ren, Microstructure and texture evolution during recrystallization of low-carbon steel sheets, J. Iron Steel Res. Int. 24 (2017) 84–90. https://doi.org/10.1016/S1006-706X(17)30012-2.

[50]   F.M. Castro Cerda, F. Vercruysse, T.N. Minh, L. Kestens, A. Monsalve, R. Petrov, The Effect of Heating Rate on the Recrystallization Behavior in Cold Rolled Ultra Low Carbon Steel, Steel Res. Int. 88 (2017) 1–9. https://doi.org/10.1002/srin.201600351.

[51]   R. Dierk, Recovery and Recrystallization: Phenomena, Physics, Models, Simulation, in: D.E. Laughlin, K. Hono (Eds.), Phys. Metall., Elsevier B.V., UK, 2014: pp. 2291–2397.

[52]   T. Gladman, On the Theory of the Effect of Precipitate Particles on Grain Growth in Metals, Proc. R. Soc. London. Ser. A. Math. Phys. Sci. 294 (1966) 298–309. http://rspa.royalsocietypublishing.org/content/294/1438/298.abstract.

[53]   R. Lagneborg, T. Siwecki, S. Zajac, B. Hutchinson, Role of vanadium in microalloyed steels, Scand. J. Metall. 28 (1999) 186–241.

[54]   H. Adrian, Thermodynamic model for precipitation of carbonitrides in high strength low alloy steels containing up to three microalloying elements with or without additions of aluminium, Mater. Sci. Technol. (United Kingdom). 8 (1992) 406–420. https://doi.org/10.1179/mst.1992.8.5.406.

[55]   P. Zhang, S.X. Li, Z.F. Zhang, General relationship between strength and hardness, Mater. Sci. Eng. A. 529 (2011) 62–73. https://doi.org/10.1016/j.msea.2011.08.061.

[56]   M. Almojil, Deformation and Recrystallisation in Low Carbon Steels, 2010.

[57]   S.J. Clark, Nano - Structuring of Micro - Alloyed Steels via Nano - Precipitate Formation, (2019).

[58]   V.S.A. Challa, W.H. Zhou, R.D.K. Misra, R. O'Malley, S.G. Jansto, The effect of coiling temperature on the microstructure and mechanical properties of a niobium-titanium microalloyed steel processed via thin slab casting, Mater. Sci. Eng. A. 595 (2014) 143–153. https://doi.org/10.1016/j.msea.2013.12.002.

[59]   R. Riva, C. Mapelli, R. Venturini, Effect of coiling temperature on formability and mechanical properties of mild low carbon and HSLA steels processed by thin slab casting and direct rolling, ISIJ Int. 47 (2007) 1204–1213. https://doi.org/10.2355/isijinternational.47.1204.

[60]   R. Song, N. Fonstein, H.J. Jun, N. Pottore, D. Bhattacharya, S. Jansto, Effects of Nb on Microstructural Evolution and Mechanical Properties of Low-Carbon Cold-Rolled Dual-Phase Steels, Metallogr. Microstruct. Anal. 3 (2014) 174–184. https://doi.org/10.1007/s13632-014-0133-9.

[61]   Y.Q. Wang, S.J. Clark, V. Janik, R.K. Heenan, D.A. Venero, K. Yan, D.G. McCartney, S. Sridhar, P.D. Lee, Investigating nano-precipitation in a V-containing HSLA steel using small angle neutron scattering, Acta Mater. 145 (2018) 84–96. https://doi.org/10.1016/j.actamat.2017.11.032.

[62]   J.M. Rodriguez-Ibabe, Thin Slab Direct Rolling of Microalloyed Steels, Trans Tech, 2007.

[63]   F.J. Humphreys, M. Hatherly, Recrystallization and Related Annealing Phenomena, Elsevier, The Netherlands, 2004. https://doi.org/10.1016/B978-008044164-1/50020-7.

[64]   H. Bhadeshia, R. Honeycombe, Steels: Microstructure and Properties, Butterworth-Heinemann, Great Britain, 2011.

[65]   H.S. Zurob, Y. Brechet, G. Purdy, A model for the competition of precipitation and recrystallization in deformed austenite, Acta Mater. 49 (2001) 4183–4190. https://doi.org/https://doi.org/10.1016/S1359-6454(01)00315-9.

[66]   T. Gladman, The physical metallurgy of microalloyed steels, Institute of Materials, London, 1997.

[67]   M. Mukherjee, U. Prahl, W. Bleck, Modelling the strain-induced precipitation kinetics of vanadium carbonitride during hot working of precipitation-hardened Ferritic–Pearlitic steels, Acta Mater. 71 (2014) 234–254. https://doi.org/https://doi.org/10.1016/j.actamat.2014.03.016.

[68]   F.S. Medina, M. Gómez, Nucleation rate and number of precipitates in V and Nb-microalloyed steels, Mater. Sci. Forum. 783–786 (2014) 1073–1078.

[69]   B. Hutchinson, Deformation microstructures and textures in steels, Philos. Trans. R. Soc. London. Ser. A Math. Phys. Eng. Sci. 357 (1999) 1471–1485. https://doi.org/10.1098/rsta.1999.0385.

[70]   R.D. Doherty, D.A. Hughes, F.J. Humphreys, J.J. Jonas, D.J. Jensen, M.E. Kassner, W.E. King, T.R. Mcnelley, H.J. Mcqueen, A.D. Rollett, Current issues in recrystallization : a review, Mater. Sci. Eng. A. 238 (1997) 219–274.

[71]   E. Hornbogen, Recrystallization of metallic materials, Metall. 27 (1973) 780–787.

[72]   H.S. Zurob, G. Zhu, S. V. Subramanian, G.R. Purdy, C.R. Hutchinson, Y. Brechet, Analysis of Mn effect on recrystallization kinetics in high Nb steels: An Example of Physically-based Alloy Design, Mater. Sci. Forum. 500–501 (2005) 123–130.

[73]   J.W. Cahn, The impurity-drag effect in grain boundary motion, Acta Metall. 10 (1962) 789–798. https://doi.org/https://doi.org/10.1016/0001-6160(62)90092-5.

[74]   H.S. Zurob, C.R. Hutchinson, Y. Brechet, G.R. Purdy, Rationalization of the softening and recrystallization behaviour of microalloyed austenite using mechanism maps, Mater. Sci. Eng. A. 382 (2004) 64–81. https://doi.org/10.1016/j.msea.2004.04.024.

[75]   A.T. Wicaksono, M. Militzer, Interaction of C and Mn in a ∑3 grain boundary of bcc iron, IOP Conf. Ser. Mater. Sci. Eng. 219 (2017) 0–8. https://doi.org/10.1088/1757-899X/219/1/012044.

[76]   S. Clark, Nano-Structuring of Micro-Alloyed Steels via Nano-Precipitate Formation, University of Warwick, 2019.

[77]   K. Ushioda, N. Yoshinaga, O. Akisue, Influences of Mn on Recrystallization Behavior and Annealing Texture Formaion in Ultralow-carbon and Low-carbon Steels, ISIJ Int. 34 (1994) 85–91. https://doi.org/10.2355/isijinternational.34.85.

[78]   M.G. Akben, I. Weiss, J.J. Jonas, Dynamic precipitation and solute hardening in A V

microalloyed steel and two Nb steels containing high levels of Mn, Acta Metall. 29 (1981) 111–121. https://doi.org/https://doi.org/10.1016/0001-6160(81)90092-4.

[79]   P.L. Mangonon, The Heat Treatment of Vanadium-Modified Alloy Steels, JOM. 33 (1981) 18–24. https://doi.org/10.1007/BF03339420.

[80]   J.H. Woodhead, Vanadium in High Strength Steels, Vanitec Publ. (1979).

[81]   H.S. ZUROB, G. ZHU, S. V SUBRAMANIAN, G.R. PURDY, C.R. HUTCHINSON, Y. BRECHET, Analysis of the Effect of Mn on the Recrystallization Kinetics of High Nb Steel: An Example of Physically-based Alloy Design, ISIJ Int. 45 (2005) 713–722. https://doi.org/10.2355/isijinternational.45.713.

[82]   M.G. Akben, T. Chandra, P. Plassiard, J.J. Jonas, Dynamic precipitation and solute hardening in a titanium microalloyed steel containing three levels of manganese, Acta Metall. 32 (1984) 591–601. https://doi.org/https://doi.org/10.1016/0001-6160(84)90070-1.

[83]   Z. Wang, X. Sun, Z. Yang, Q. Yong, C. Zhang, Z. Li, Y. Weng, Effect of Mn concentration on the kinetics of strain induced precipitation in Ti microalloyed steels, Mater. Sci. Eng. A. 561 (2013) 212–219. https://doi.org/10.1016/j.msea.2012.10.085.

[84]   M.R. Toroghinezhad, A.O. Humphreys, E. Essadiqi, F. Ashrafizadeh, A. Najafizadeh, J.J. Jonas, Effect of chromium, boron and manganese additions on the deformation and recrystallization textures of warm rolled low carbon steels, ISIJ Int. 43 (2003) 1842–1850. https://doi.org/10.2355/isijinternational.43.1842.

[85]   H. Abe, T. Suzuki, S. Okada, Decomposition of Mn-C Dipoles during Quench-Ageing in Low-Carbon Aluminium-Killed Steels, Trans. Japan Inst. Met. 25 (1984) 215–225. https://doi.org/10.2320/matertrans1960.25.215.

[86]   V. Massardier, E. Le Patezour, M. Soler, J. Merlin, Mn-C interaction in Fe-C-Mn steels: Study by thermoelectric power and internal friction, Metall. Mater. Trans. A Phys. Metall. Mater. Sci. 36 (2005) 1745–1755. https://doi.org/10.1007/s11661-005-0039-x.

[87]   H. Numakura, G. Yotsui, M. Koiwa, Calculation of the strength of Snoek relaxation in dilute ternary B.C.C. alloys, Acta Metall. Mater. 43 (1995) 705–714. https://doi.org/https://doi.org/10.1016/0956-7151(94)00262-G.

[88]   H. Saitoh, K. Ushioda, Influences of Manganese on Internal Friction and Carbon Solubility Determined by Combination of Infrared Absorption in Ferrite of Low-carbon Steels, ISIJ Int. 29 (1989) 960–965. https://doi.org/10.2355/isijinternational.29.960.

[89]   H. Saitoh, N. Yoshinaga, K. Ushioda, Influence of substitutional atoms on the Snoek peak of carbon in b.c.c. iron, Acta Mater. 52 (2004) 1255–1261. https://doi.org/10.1016/j.actamat.2003.11.009.

[90]   F.B. Pickering, Physical metallurgy and the design of steels, Applied Science Publishers, 1978.

[91]   H.J. Kestenbach, S.S. Campos, E. V. Morales, Role of interphase precipitation in microalloyed hot strip steels, Mater. Sci. Technol. 22 (2006) 615–626. https://doi.org/10.1179/026708306X81487.

[92]   Y. Ateba Betanda, A.L. Helbert, F. Brisset, M.H. Mathon, T. Waeckerlé, T. Baudin, Measurement of stored energy in Fe-48%Ni alloys strongly cold-rolled using three approaches: Neutron diffraction, Dillamore and KAM approaches, Mater. Sci. Eng. A. 614 (2014) 193–198. https://doi.org/10.1016/j.msea.2014.07.037.

[93]   P. Köhnen, M. Létang, M. Voshage, J.H. Schleifenbaum, C. Haase, Understanding the process-microstructure correlations for tailoring the mechanical properties of L-PBF produced austenitic advanced high strength steel, Addit. Manuf. 30 (2019) 100914. https://doi.org/https://doi.org/10.1016/j.addma.2019.100914.

[94]   R.D.K. Misra, H. Nathani, J.E. Hartmann, F. Siciliano, Microstructural evolution in a new 770MPa hot rolled Nb–Ti microalloyed steel, Mater. Sci. Eng. A. 394 (2005) 339–352. https://doi.org/https://doi.org/10.1016/j.msea.2004.11.041.